



저작자표시-비영리-변경금지 2.0 대한민국

이용자는 아래의 조건을 따르는 경우에 한하여 자유롭게

- 이 저작물을 복제, 배포, 전송, 전시, 공연 및 방송할 수 있습니다.

다음과 같은 조건을 따라야 합니다:



저작자표시. 귀하는 원저작자를 표시하여야 합니다.



비영리. 귀하는 이 저작물을 영리 목적으로 이용할 수 없습니다.



변경금지. 귀하는 이 저작물을 개작, 변형 또는 가공할 수 없습니다.

- 귀하는, 이 저작물의 재이용이나 배포의 경우, 이 저작물에 적용된 이용허락조건을 명확하게 나타내어야 합니다.
- 저작권자로부터 별도의 허가를 받으면 이러한 조건들은 적용되지 않습니다.

저작권법에 따른 이용자의 권리는 위의 내용에 의하여 영향을 받지 않습니다.

이것은 [이용허락규약\(Legal Code\)](#)을 이해하기 쉽게 요약한 것입니다.

[Disclaimer](#)

공학박사 학위논문

DEVELOPMENT OF BRAIN-MACHINE
INTERFACE TRAINING SYSTEM AND
ITS APPLICATION TO ROBOTIC ARM CONTROL
USING NON-INVASIVE NEURAL SIGNAL

비침습적 뇌 신호를 이용한 로봇팔
제어를 위한 뇌-기계 인터페이스
훈련시스템의 개발 및 적용

2018 년 8 월

서울대학교 대학원

협동과정 바이오엔지니어링 전공

김 윤 재

DEVELOPMENT OF BRAIN-MACHINE
INTERFACE TRAINING SYSTEM AND
ITS APPLICATION TO ROBOTIC ARM CONTROL
USING NON-INVASIVE NEURAL SIGNAL

비침습적 뇌 신호를 이용한 로봇팔
제어를 위한 뇌-기계 인터페이스
훈련시스템의 개발 및 적용

지도교수 김 성 완

이 논문을 공학박사 학위논문으로 제출함

2018 년 5 월

서울대학교 대학원
협동과정 바이오엔지니어링 전공
김 윤 재

김윤재의 공학박사 학위논문을 인준함

2018 년 6 월

위원장	박 광 석	(인)
부위원장	김 성 완	(인)
위원	방 문 석	(인)
위원	정 선 근	(인)
위원	박 형 순	(인)

Ph. D. Dissertation

DEVELOPMENT OF BRAIN–MACHINE
INTERFACE TRAINING SYSTEM AND
ITS APPLICATION TO ROBOTIC ARM CONTROL
USING NON–INVASIVE NEURAL SIGNAL

BY

YOON JAE KIM

AUGUST 2018

INTERDISCIPLINARY PROGRAM IN BIOENGINEERING
THE GRADUATE SCHOOL
SEOUL NATIONAL UNIVERSITY

DEVELOPMENT OF BRAIN-MACHINE
INTERFACE TRAINING SYSTEM AND
ITS APPLICATION TO ROBOTIC ARM CONTROL
USING NON-INVASIVE NEURAL SIGNAL

BY

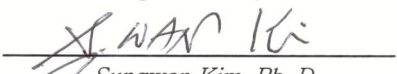
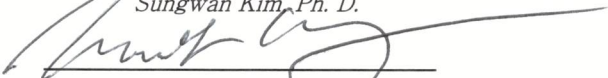
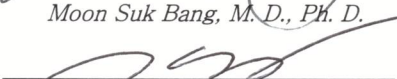
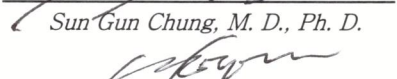
YOON JAE KIM

INTERDISCIPLINARY PROGRAM IN BIOENGINEERING
THE GRADUATE SCHOOL
SEOUL NATIONAL UNIVERSITY

THIS DISSERTATION IS APPROVED FOR
THE DEGREE OF DOCTOR OF
PHILOSOPHY

JUNE 2018

DOCTORAL COMMITTEE:

Chairman	 <i>Kwang Suk Park, Ph. D.</i>
Vice Chairman	 <i>Sungwan Kim, Ph. D.</i>
Member	 <i>Moon Suk Bang, M. D., Ph. D.</i>
Member	 <i>Sun Gun Chung, M. D., Ph. D.</i>
Member	 <i>Hyung-Soon Park, Ph. D.</i>

Abstract

DEVELOPMENT OF BRAIN–MACHINE INTERFACE TRAINING SYSTEM AND ITS APPLICATION TO ROBOTIC ARM CONTROL USING NON–INVASIVE NEURAL SIGNAL

By

Yoon Jae Kim

Interdisciplinary Program in Bioengineering
The Graduate School
Seoul National University

People can face losing all or part of their motor functions because of various diseases or physical accidents such as spinal cord injury (SCI), stroke, and amyotrophic lateral sclerosis. The damage to motor functions frequently makes it difficult to perform activities of daily living (ADL). Therefore, various engineering technologies have been developed to help patients who have lost motor functions. Lost motor ability can be recovered in two types of robot based approaches. One of these approaches is robot based training for the rehabilitation of a patient's motor functions. Generally, rehabilitation training is performed with the assistance of a physical therapist, but rehabilitation robots have been developed to save labor input and to provide more repetitive and quantitative training. When the degree of damage is so severe that the rehabilitation of a motor function is difficult, it is more

appropriate to replace the motor function with a robotic prosthesis, which is controlled by bio-signals that reflect the user's intentions. Bio-signals such as electromyogram (EMG) and neural signals provide features for human intention analysis. This study especially focuses on robotic arm control based on neural signal analysis, which allows the user to bypass the conventional pathways of motor control, and is expected to have a wide range of applications. Development of a robotic arm system controlled by a non-invasive neural signal induced from motor imagery of arm movement has been one of the especially challenging goals of the brain-machine interface (BMI) field. In this research, three steps have been attempted to approximate the goal.

In the first step, a hand velocity vector was estimated based on the movement of a real arm. A "preferred direction (PD)" based decoding model is not appropriate for electroencephalogram (EEG) since its spatial resolution cannot reach the neuron level. Thus, a linear model for hand velocity prediction was considered, and the possibility of the model was verified by the estimation of the real hand trajectory of a normal user. The subject would reach his/her hand to a target point and return it to the original position, and the neural signal and the actual velocity vector of the hand were measured simultaneously for multiple linear regressions. EEG and magnetoencephalogram (MEG) were applied, and parameters for prediction were estimated using the least squares method. The correlation coefficient (CC) between the predicted and real trajectories in the case of MEG was 0.705 ± 0.292 ($p < 0.001$). In the case of EEG, the CC was 0.684 ± 0.231 ($p < 0.001$). When the robot was preprogrammed to grasp the target object at the closest position, the success rates in grasping the target object were 18.75% and 7.50% for MEG and EEG, respectively. The success rates of touching were respectively 52.50% and 58.75%.

In the second step, a novel training system, which can improve motor imagery ability and determine decoding parameters for patients with paralyzed upper

limb, was proposed and developed. Even though the conventional shared control based training systems exhibited effective training performance, they are limited to predetermined targets and tasks provided by the training system. In this study, the previous algorithm was modified and additional functionality was added by using an RGB-D camera. Multiple targets can be detected and the positions estimated automatically. Furthermore, user intended targets are selected automatically and the active shared control attracts the robot end-effector to the intended target. Thus, the user can select which target to reach by his/her own volition without any preprogrammed information. Kinect with camera calibration estimated the target position with a distance error of $4.620 \pm 3.490\%$. When the developed algorithm with appropriate blending parameters ($\alpha = \beta = 0.60$) was applied to pre-recorded trajectories, the distance error to an intended target decreased by 51.85%.

In the final step, to observe the effectiveness of the developed system, two subjects with cervical SCI were trained to use the system. After 5 training sessions with the developed system, functional magnetic resonance imaging showed brain activation patterns with a tendency of focusing on the ipsilateral primary motor and sensory cortex, posterior parietal cortex, and contralateral cerebellum.

Through this study, a linear decoding model for hand velocity estimation was verified and a vision-aided BMI training system was developed. Based on the developed training system, subjects with cervical SCI showed brain activation patterns with a tendency toward meaningful focusing.

Keywords: Motor function, Spinal cord injury, Brain-machine interface, Electroencephalogram, Training system, Shared Control, Functional magnetic resonance imaging.

Student number: 2014-21552

Contents

Abstract	i
Contents.....	iv
List of Tables	vii
List of Figures	viii
1. Introduction	1
1.1. Robots for Motor Function Recovery.....	1
1.2. Neural Signal Based Robotic Arm Control	2
1.2.1. Brain-Machine Interface.....	2
1.2.2. Previous Robotic Arm Control Methods	7
1.2.3. Shared Control Strategies for Training.....	15
1.3. Objectives and Scope	21
2. Materials and Methods	25
2.1. Hand Velocity Estimation of Real Arm Movement.....	25
2.1.1. Overview	25
2.1.2. Signal Acquisition and Processing	27
2.1.3. Robotic Arm Hardware	33

2.1.4.	Performance Verification.....	37
2.2.	Development of Vision-Aided Training System	42
2.2.1.	System Overview	42
2.2.2.	Target Object Detection and Camera Calibration	44
2.2.3.	Training System Hardware.....	54
2.2.4.	Shared Control Strategy	57
2.3.	Clinical Application and fMRI Evaluation.....	63
3.	Results	68
3.1.	Performance of Hand Trajectory Prediction.....	68
3.2.	Performance of Vision-Aided Training System	81
3.2.1.	Target Object Detection and Position Estimation	81
3.2.2.	Trajectory Compensation	83
3.3.	Effect of Training System in Two Clinical Cases.....	90
4.	Discussion	92
4.1.	Evaluation for Hand Velocity Estimation.....	92
4.2.	Evaluation for Vision-Aided Training System	96

5. Conclusion	102
References	104
Abstract in Korean	117
Acknowledgement	120

List of Tables

Table 2.1 Denavit-Hartenberg parameters for the robotic arm.....	62
Table 3.1 Accuracy of the trajectories predicted with MEG	71
Table 3.2 Accuracy of the trajectories predicted with EEG	74
Table 3.3 Comparison of MEG and EEG	76
Table 3.4 Success rates for grasping and touching	79
Table 3.5 Accuracy of the position estimation	82
Table 3.6 Improvement of the predicted hand trajectory.....	88
Table 4.1 Improvement of the predicted hand trajectory at $\alpha = \beta =$ 0.60 and 1.00	99

List of Figures

Figure 1.1 Spatiotemporal scales of various neural signal types.....	4
Figure 1.2 Seven-DOF robotic arm controlled using MEA.	8
Figure 1.3 Full brain-control of the modular prosthetic limb (MPL). (a) 7D sequence task. Translation targets are indicated by an LED light and text indicates the orientation and grasp targets. (b) Action Research Arm Test (ARAT). (c) The cone-stacking task. (d) Side-by-side comparisons showing the participant using the robotic arm to grasp an object with different approach angles.....	9
Figure 1.4 Utah Electrode Array.....	10
Figure 1.5 Experimental environment without visual stimulation.	13
Figure 1.6 Two types of BMI training for robotic arm control. (a) observation-based training. (b) shared control based training. The training approaches consist of user training for the adaptation of motor imagery and parameter training for improved decoding performance.	20
Figure 1.7 Overall research flow. The current study consists of 3 steps. Model verification using ECoG is not treated because the invasive approach is not the focus of this study.	24
Figure 2.1 Signal processing procedure. Training has to be conducted to	

obtain the weight matrices. The filtering, down-sampling, and linear regression processes are explained in the *Movement prediction* section.26

Figure 2.2 Rotational transformation to change trajectories in the accelerometer coordinates to IRAGS coordinates. (a) Predicted hand trajectories reconstructed from neural signal before transformation. (b) Predicted hand trajectories after transformation. * Abbreviation: Integrated robotic arm-gripper system (IRAGS).32

Figure 2.3 Integrated robotic arm-gripper system (IRAGS). (a) Hardware of the IRAGS. The IRAGS consists of a six-DOF robotic arm, adaptive robotic gripper, and mechanical coupling. (b) Mechanical coupling to connect the six-DOF robotic arm and adaptive robotic gripper.34

Figure 2.4 Five-fold cross validation for hand trajectory prediction. In the five-fold cross validation process, the test data, which guarantee generalizability, is obtained.39

Figure 2.5 Overall flow of the proposed BMI training system. The solid line represents the flow of the signal, and the dotted line represents the model and parameters used.43

Figure 2.6 Procedure for target object detection. (a) RGB image obtained from Kinect. (b) Binary image. (c) Noise-filtered

image. (d) Object detection via hierarchical clustering.	46
Figure 2.7 (a) Distortion between RGB and depth images caused by location of the sensors. (b) The same image photographed by the RGB (left) and depth (right) cameras, respectively.	48
Figure 2.8 (a) calibration for distance estimation. (b) calibration for x and y coordinates estimation.	51
Figure 2.9 Experimental setup to validate camera calibration for position estimation.....	53
Figure 2.10 (a) BMI training system, consisting of a robotic arm, Kinect, and targets. (b) Frames and variables of the robotic arm kinematics.....	56
Figure 2.11 Training setup. (a) Virtual reality based training for the first 5 sessions. (b) Observation-based training for the last 5 sessions. After each observation-based training, shared control based reaching target was attempted to confirm improved decoding performance.	65
Figure 2.12 Overall plan of clinical application.....	66
Figure 3.1 Trajectories predicted from neural signals and real trajectories. (a) Hand trajectories predicted by MEG (first session of subject 4). (b) Real hand trajectories reconstructed from the accelerometer signal during MEG	

signal acquisition (first session of subject 4). (c) Hand trajectories predicted by EEG (first session of subject 7). (d) Real hand trajectories reconstructed from the accelerometer signal during EEG signal acquisition (first session of subject 7). Each color represents one of the four hand-movement directions.....70

Figure 3.2 TPE of MEG and EEG. (a) The distance between the target sphere and adaptive robotic gripper was 30 cm. The radius of the TPE is the average distance between the target sphere and adaptive robotic gripper at the closest position. (b) Miniaturized drawing of the real BMI system. Lengths are proportional to the actual size. * Abbreviation: terminal point error (TPE).....72

Figure 3.3 Grasping and touching the target object. (a) Grasping. (b) Touching. (c) Failure.80

Figure 3.4 (a) Compensated trajectory (red) reaches more closely to the target object than the raw hand trajectory predicted from EEG. (b) Definition of the joint angles of the robotic arm. (c) Green line indicates the ideal joint angle to reach the target object. Joint angles are closer to the ideal joint angles with compensation (red) than without (blue).84

Figure 3.5 (a) Decreased error to the intended target averaged over all

120 trials. Points with blending parameters $(\alpha, \beta) = (0.60, 0.60)$ and $(1.00, 1.00)$ are represented. (b) Decreased error to intended target averaged over 30 trials for individual directions.....85

Figure 3.6 (a) Decreased error to the three non-intended targets averaged over 120 trials. (b) Decreased error to the three non-intended targets averaged over 30 trials for each direction.87

Figure 3.7 (a) Raw hand trajectories predicted from EEG. (b) Compensated hand trajectories using artificial potential....89

Figure 3.8 (a) fMRI image during reaching task (left arm) in subject #1 shows brain activation in various area including right primary motor and sensory cortex, posterior parietal cortex, prefrontal cortex, and left cerebellum ($p < 0.001$). (b) Brain activation is relatively focused to the right primary motor and sensory cortex, posterior parietal cortex, and left cerebellum after 5 sessions of BMI training ($p < 0.001$)....91

1. Introduction

1.1. Robots for Motor Function Recovery

Motor function impairment can be caused by issues such as spinal cord injury (SCI), stroke, amyotrophic lateral sclerosis, etc. The recovery of motor functions conventionally includes not only clinical rehabilitation but also the replacement of severely impaired motor functions. Robots for motor function rehabilitation usually focus on the patients with motor disabilities, which have possibility of clinical recovery. Since the end of the 1990s, there has been substantial interest in research on the development of robotic devices for rehabilitation, especially for the neurorehabilitation of poststroke patients. Early research on robotic therapy for the upper limb utilized the end-effector type, but since around the mid-2000s, more researchers have focused on the exoskeleton type due to its advantages. Exoskeleton types are wearable structures and advantageous in the determination of individual anatomical joint configuration. Even though previous studies have reported the efficacy of rehabilitation robots, patients with severe injury to motor functions need a replacement of the upper limb rather than rehabilitation. Robotic arm control for motor function replacement usually depends on bio-signals induced by user intentions. Bio-signals such as electromyogram (EMG) and neural

signals can provide the user's motor intention via various pattern recognition approaches. Whereas neural signal based robotic arm control is almost always focused on scientific purposes because it requires invasive procedures of electrode implantation for robust performance, EMG is probably the most widely used type of bio-signal both in commercial products and in scientific research [1]. Each type of signal has its own advantages and disadvantages and an approach should be selected by considering various factors such as type of disease/injury, cost, safety, etc.

1.2. Neural Signal Based Robotic Arm Control

1.2.1. Brain-Machine Interface

Paralysis following SCI, stroke, amyotrophic lateral sclerosis and various other disorders can disconnect the brain from the body, and eliminate the ability to perform voluntary movements [2]. Various technologies have been developed to help people replace lost motor function. Among these technologies, brain-machine interfaces (BMIs), which depend on features from users' neural signals, enable control of external devices such as robotic

arms and computer cursors. BMIs allow a person to bypass conventional neuromuscular pathways to interact with the environment.

Different types of neural signals vary in the accuracy and resolution of their information transmission. Generally, there is trade-off, having increased the accuracy and resolution of recorded neural signals at the expense of increased invasiveness [3]. The spatial and temporal resolution of each signal type is summarized in Fig. 1.1.

Electroencephalogram (EEG) is a non-invasive neural signal measured from a population of underlying cortical neurons using electrodes placed on the scalp [3]. Because of its non-invasiveness, EEG is widely acceptable for signal acquisition for a human application. The features can be extracted from various frequency bands such as delta (< 4 Hz), theta (4~8 Hz), mu (8~12 Hz), beta (12~30 Hz), and gamma (30~100 Hz) [4]. The limited spatial resolution of EEG degrades the performance of external devices such as neuroprosthetic limbs, and has thus faced signal processing for its slow real-time decoding of user intent [5]. Additionally, artifacts and noise can cause disturbances in the signal due to the electrodes' position on the scalp. The quality of EEG deteriorates as the signal passes through the skull and skin to reach the external electrodes. Another non-invasive neural signal, magnetoencephalogram (MEG), is a record of magnetic fields, induced by electrical neural activation. MEG electrodes are fixed into a helmet in which the user places their head during the measurement. The magnetic fields are formed by the same underlying electrical activations that produce the EEG.

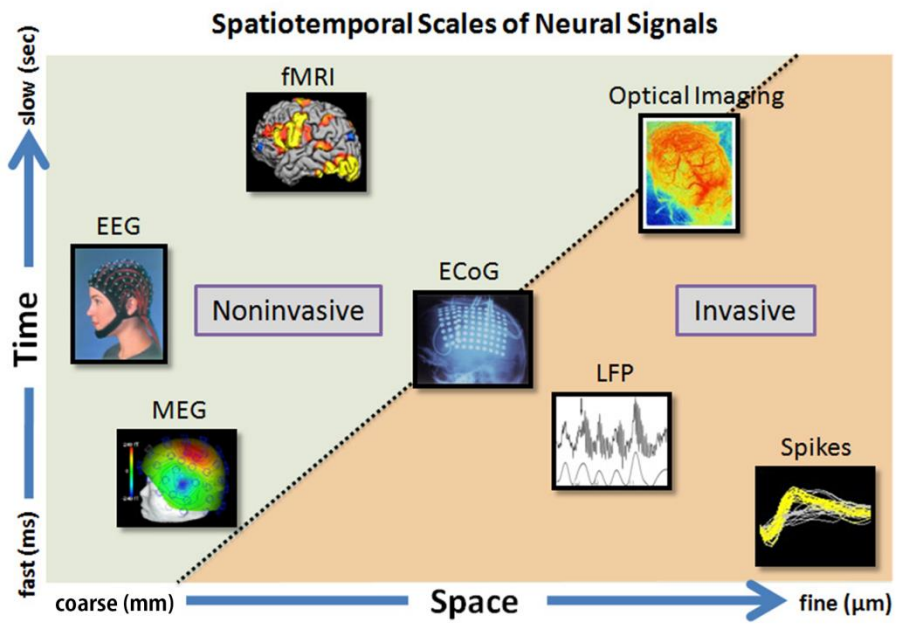


Fig. 1.1 Spatiotemporal scales of various neural signal types [6].

Electrocorticogram (ECoG) demonstrates a higher signal to noise ratio (SNR) due to the placement of electrodes on the cortex, either subdurally or epidurally. So, ECoG can provide not only a higher signal quality but also a wider frequency band for signal acquisition [3]. Nevertheless, the implantation of ECoG electrodes requires craniotomy (a surgical incision into the skull) and is therefore limited to patients with clinical reasons such as localization of epileptogenic zones.

Invasive electrodes record action potentials from a single or a population of neurons [4]. Spike is a neural signal type that provides the finest spatial and temporal resolution. A microelectrode array (MEA) can record action potentials from multiple neurons surrounding it. Spikes are generally filtered with a frequency band on 300~5,000 Hz range, and their shapes are highly dependent on the geometry and location of electrode. Although spikes provide the most improved performance for neuroprosthetic control, they require implantation surgery which can be burdensome for users. Thus, high reliability for the decoding technique should be assured. Furthermore, the rigidity of MEA makes it susceptible to shift from its initial location due to the micromotion of soft brain tissue [7, 8]. This renders the original decoding parameters useless. MEA can also cause issues with biocompatibility, which is a characteristic highly related with the longevity of the BMI system. Glial cells encapsulate microelectrodes a few weeks after implantation and increase impedance, which prevents signal acquisition [8, 9]. Another type of signal

measured by MEA, local field potential (LFP) can be considered. LFP is recorded by changing the frequency band to a lower range (< 250 Hz) [4].

The various neural signal types (EEG, MEG, ECoG, Spikes, and LFP) above have advantages and disadvantages, and appropriate signals should be selected by considering the purpose, required accuracy and acceptable invasiveness of the target BMI system.

Recently, BMI systems are considered to be applied to not only the replacement of human motor functions but also rehabilitation due to the plasticity of the spinal cord. Even in patients with motor complete SCI, there are still remaining spinal connections across the injury site, though these preserved connections are not sufficient to transfer voluntary movement [10]. The voluntary movement can be partially recovered when electrical stimulation is provided to spinal cord [11, 12]. The connections reawakened by electrical stimulation can be more permanent when a physical activity based therapy is added [13, 14]. In this regard, a BMI that extracts a motor intention to provide the appropriately timed spinal cord stimulation can be an improved way to induce plasticity of spine along with the activity-dependent plasticity seen in physical rehabilitation [4]. This system provides a causal relationship between the paralyzed limb and brain and may enhance the synaptic strength of the remaining neural connections across the injury site [15-17]. Even though the BMI based spinal cord stimulation is not yet applied to clinical treatment, it is expected that the control of the spinal cord using BMI could provide an improved rehabilitation efficacy of motor function.

1.2.2. Previous Robotic Arm Control Methods

Upper limb control is one of the most important abilities of a person, and replacing a lost motor function of the upper limb is a crucial goal. Thus, since the concept of BMIs was first proposed, scientists and engineers have improved upon the technology for developing a human-controlled external robotic arm that does not require physical movement [18-21]. Monkeys have fed themselves by controlling a robotic arm [22], and humans have utilized invasive neural signals to control a seven degrees of freedom (DOF) robotic arm as if it were their own [2, 23]. Previous notable studies [2, 23] showed that the success rate of reaching and grasping can reach about 70~90% in an allocated time. In these studies, tetraplegia subjects participated and controlled the robotic arm and hand over a broad workspace using spikes recorded from neurons of motor cortex by using one or two 96-channel MEAs. One of the participants, implanted with the electrodes 5 years earlier, was able to drink coffee in a bottle (Fig. 1.2) [2]. Furthermore, various target-based tasks were performed (Fig. 1.3) [23]. In these tasks, it was possible not only to grab and move objects, but also to approach the same objects from various orientations. These studies used intracortical MEA, which are highly invasive (Fig. 1.4). Features of the spikes measured from MEA provide a high spatial resolution, which is advantageous in the accurate prediction of imagery hand velocity.



Fig. 1.2 Seven-DOF robotic arm controlled using MEA [2].
(Figure courtesy of Springer Nature, license number: 4365710111201)

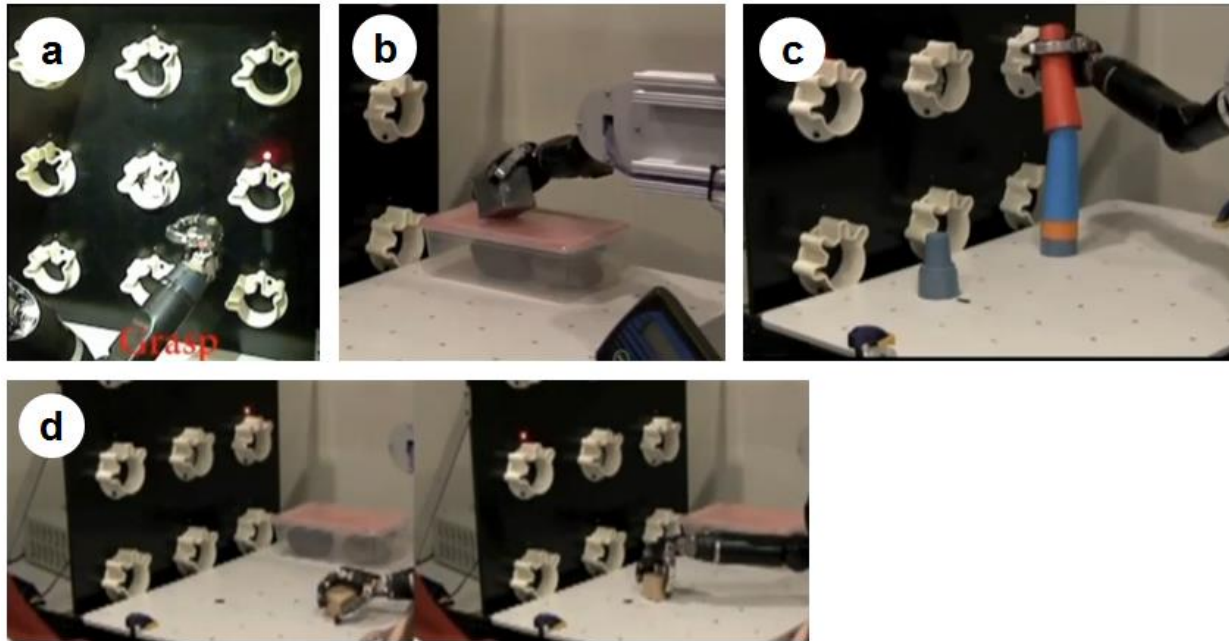


Fig. 1.3 Full brain-control of the modular prosthetic limb (MPL). (a) 7D sequence task. Translation targets are indicated by an LED light and text indicates the orientation and grasp targets. (b) Action Research Arm Test (ARAT). (c) The cone-stacking task. (d) Side-by-side comparisons showing the participant using the robotic arm to grasp an object with different approach angles [23]. (Figure courtesy of Elsevier, license number: 4365720833797)

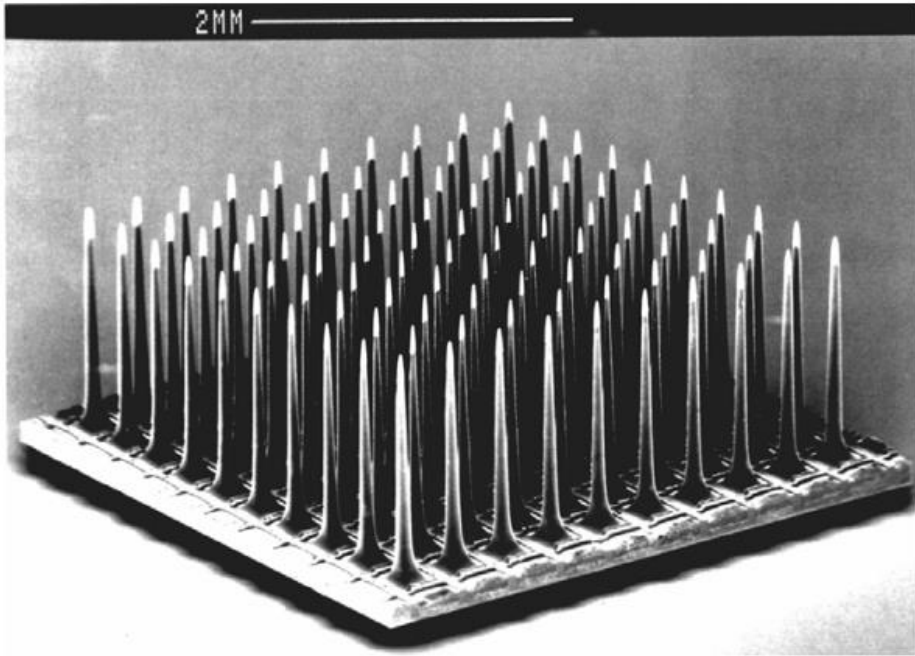


Fig. 1.4 Utah Electrode Array [24].

(Figure courtesy of Springer Nature, license number: 4365730647713)

Even though approaches based on MEA are highly successful, many researchers still attempt to control a robotic arm with non-invasive neural signals, such as EEG, which do not require surgically implanting an electrode array. Previous EEG studies for robotic arm control used features such as P300 [25-28], N2pc [26, 28], steady-state visual evoked potential (SSVEP) [29-32], and mental task differentiation [26, 33-37].

The P300 wave is an event related potential component utilized in the process of decision making. P300 is a potential evoked by an awaited infrequent event (odd-ball paradigm) and it features a positive peak produced approximately 300 ms after receiving a visual stimulus [26]. P300 is usually detected by electrodes over the central areas of the scalp [38, 39]. This response spreads out to almost area of the brain cortex with decreased amplitude. Another evoked potential is N2pc, which is a negative peak over the visual cortex produced approximately 200 ms after a visual stimulus [26]. P300 and N2pc based robotic arm control requires a visual stimulator, and the odd-ball paradigm proposed by Farewell and Donchin [40] has been used as is or modified to provide the stimulation.

SSVEP is a natural response to a visual stimulus that vibrates at a specific frequency. When a visual stimulus ranging from 3.5 Hz to 75 Hz is provided, the brain produces electrical activity at the same frequency of the stimulus [41]. For example, consider three light sources that are flickering at distinct frequencies of 5 Hz, 7 Hz, and 9 Hz. The SNR for each possible stimulation frequency is measured and the highest SNR indicates which light stimulator

the user is focusing on [29]. By letting each light stimulator encode a preprogrammed command, for example 'up', 'down', 'left', and 'right', the interface can be utilized to control an external robotic arm.

Spontaneous BMI systems conduct preprogrammed commands when the user thinks of specific mental tasks [26]. According to previous research, the neural activity of imagined and actual motor movements follow the same pattern [42]. Moreover, an intended motion can be conducted by mapping the motion to the preprogrammed mental task (concentration tasks), which is actually not related with the motion. For example, Hortal mapped four mental tasks to corresponding robotic movements (Fig. 1.5) [33]. Two motor tasks (open/close of right and left hand) and two concentration tasks (numerical and alphabetical exercises) were mapped with a horizontal plane movement of a robotic arm end-effector. For classification, frequency domain features from a 3-second windowed segment were utilized and support vector machine was used as the classifier. Two users for this BMI system successfully controlled the robotic arm to reach four targets, although it takes two to three minutes to reach each goal once. The mental task based control is advantageous in that it does not require visual stimulation compared to other evoked potential-based approaches.

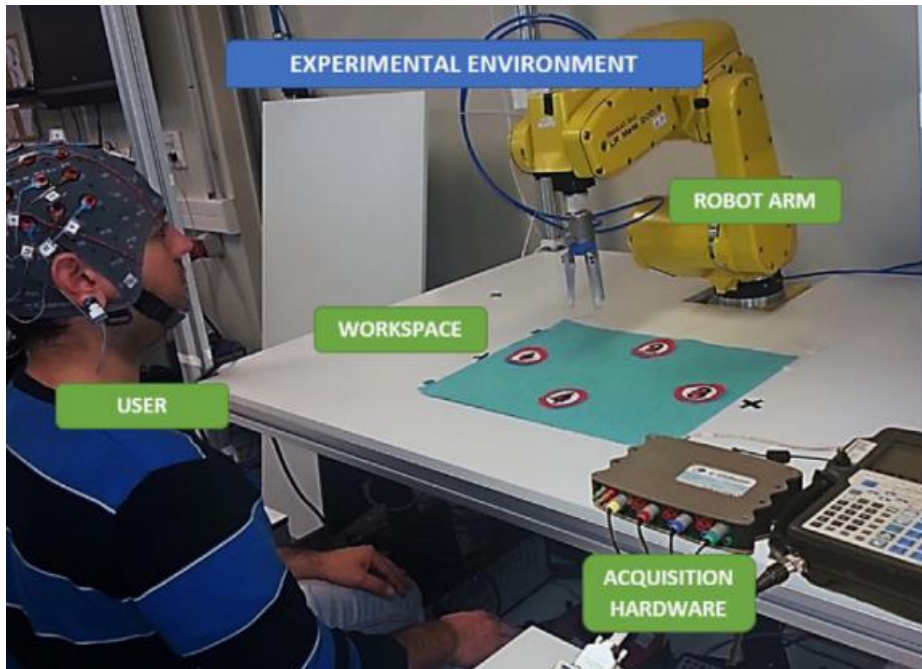


Fig. 1.5 Experimental environment without visual stimulation [33].
(Figure courtesy of Elsevier, license number: 4365730098234)

In many cases, the BMI system for robotic arm control uses auxiliary sensor and assistance for easier control. The blending of sensor information and neural signals for a more intelligent system has been applied to the BMI field for the improvement of task performance or fine control of terminal devices. Kim et al. [43] controlled a robotic arm with the aid of external sensors and greatly improved the performance of reaching and grasping motions. Downey et al. [44] exhibited that an RGB-D camera is effective in compensating the trajectory of a robotic arm and improving performance. McMullen et al. reported a semi-autonomous hybrid BMI using ECoG, eye tracking and computer vision [45]. Kapil et al. demonstrated a collaborative brain-computer interface approach using a dexterous robotic manipulator, Kinect, and MEA [46].

1.2.3. Shared Control Strategies for Training

Decoding Model and Its Parameters

In motor imagery based robotic arm control, appropriate decoding models and the determination of related parameters are key elements for successful system implementation. Previous invasive studies have used the concept of cosine tuning for decoding models, and this idea was first proposed by Georgopoulos et al. [47]. The model describes the firing rate of individual neurons with respect to the direction of hand movements such that neuron fire at a maximal rate when the hand is moving in the “preferred direction (PD)” of the neuron [48]. In the PD tuning model, the 3D hand velocity direction v is related to the firing rate λ_i of neuron i by the tuning parameter (preferred direction vector) $\beta_i = [\beta_{ix} \beta_{iy} \beta_{iz}]$, offset by the neuron’s baseline firing rate β_0 . The scalar PD model is represented by the equation below (residual values related to noise are not expressed) [48].

$$\lambda_i = \beta_{ix}v_x + \beta_{iy}v_y + \beta_{iz}v_z + \beta_0 \quad (1.1)$$

Based on the PD model, the population vector algorithm (PVA) was proposed to reconstruct or predict movement directions from the firing rates of a population of directionally tuned neurons. It is a voting strategy in which the predicted direction of movement p is formed by summing a contribution from each neuron in its normalized PD scaled by w_i .

$$w_i = \lambda_i - \beta_{i0} \quad (1.2)$$

$$p = \sum_i w_i \frac{\beta_i}{\|\beta_i\|} \quad (1.3)$$

When the model is expanded for seven-DOF motion, it is expressed as follows [23]. The 3 parameters for translational motion $\beta_i = [\beta_{ix} \beta_{iy} \beta_{iz}]$, 3 parameters for rotational motion $\beta_{\vartheta i} = [\beta_{\vartheta ix} \beta_{\vartheta iy} \beta_{\vartheta iz}]$, and 1 parameter for grasping motion β_{ig} are individually trained to prevent a nonlinearly coupled effect between different types of motions [48]. Parameter vectors β_i and $\beta_{\vartheta i}$ indicate linear and rotational preferred directions, respectively.

$$\lambda_i = \beta_{ix}v_x + \beta_{iy}v_y + \beta_{iz}v_z + \beta_{i\vartheta x}v_{\vartheta x} + \beta_{i\vartheta y}v_{\vartheta y} + \beta_{i\vartheta z}v_{\vartheta z} + \beta_{ig}v_g + \beta_{i0} \quad (1.4)$$

Indirect optimal linear estimation (OLE) and ridge regression are used to estimate the parameters of seven-DOF PD models due to the many-to-one relationship of movement parameters to firing rates [23, 49].

Shared Control for BMI Training System

For the determination of the parameters of the decoding model and user adaptation to the model (co-adaptive process), training sessions are required. As reported in previous robotic arm control studies applied to non-human primates [48] and humans [23], the training process can proceed in two phases. In the first phase, observation-based training is provided. During the phase, the robotic arm moves automatically driven by preprogrammed algorithm (artificial source) to reach targets and an initial decoder is generated (Fig. 1.6(a)). In the second phase of calibration, the user controls the robotic arm by using the initial decoder while the shared control strategy assists the reaching motion (Fig. 1.6(b)). An improved decoder can be built from the second phase.

During the second phase of training or the initial stage of test control, the shared control strategy can assist the robotic arm control to motivate user by maintaining the success rate to certain level. Two types of shared control, which have been used in previous studies [23, 48], are introduced in this section because the purpose is highly similar to that of this study.

The first type (passive shared control) uses ortho-impedance, which suppresses the brain-command component perpendicular to the ideal direction. The algorithm is computed as the equations shown below [50]. Vector v indicates the output command, and u indicates the user's control command. The vectors $S(D, u)$ and $K(D, u)$ are the projection and orthogonal components of the collection matrix of desired directions D . \hat{D} is the set of column vectors from D with the largest magnitude of unique positive projections on to u , and was proposed by Clanton [48].

$$v = (S(D, u) + \alpha_1 K(D, u))u \quad (1.5)$$

$$S(D, u) = \hat{D}(\hat{D}^T \hat{D})^{-1} \hat{D}^T \quad (1.6)$$

$$K(D, u) = I - S(D, u) \quad (1.7)$$

As the elements of $n \times n$ diagonal matrix α_1 increase, errors with the orthogonal component also increase. Thus, this parameter determines the error admittance of the training system.

The second type (active shared control) directly mixes a user's control commands u with the command from an artificial source d to produce the mixed control command v as the equation suggested below [43, 48].

$$v = \alpha_2 u + (I - \alpha_2)d \quad (1.8)$$

The $n \times n$ diagonal matrix α_2 is a blending parameter, and the proportion of control shared by the artificial source increases as the elements of α_2 decrease. The diagonal elements' values range from 0 to 1, and it is possible to design these elements to have the same values.

A recent study, which reported a human controlled 7-DOF robotic arm, utilized the introduced algorithms during the second phase of training and the initial learning phase of the task (up to day 66). The shared control algorithm highly contributed to improving the parameters of the decoder and user adaptation for motor imagery.

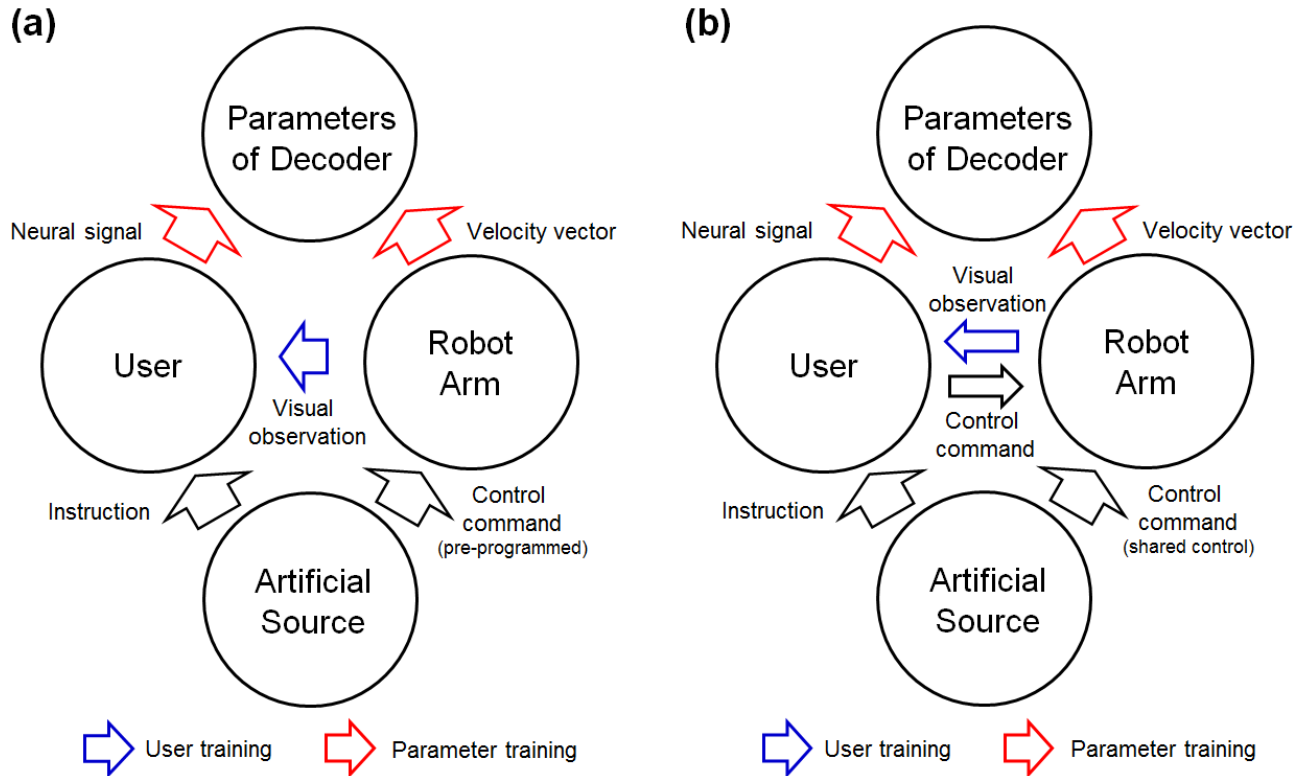


Fig. 1.6 Two types of BMI training for robotic arm control. (a) observation-based training. (b) shared control based training. The training approaches consist of user training for the adaptation of motor imagery and parameter training for improved decoding performance.

1.3. Objectives and Scope

Although conventional robotic arm control approaches based on EEG have demonstrated high performance in terms of accuracy, they are relatively unintuitive, inefficient in terms of time, and mostly require additional interfaces for visual stimulation. Thus, the hand velocity predicted from EEG activated by motion-related motor imagery can be considered as an ultimate substitution for conventional EEG based control. Even though some research using mental task differentiation [26, 33-37] exhibited robotic arm control based on motor imagery, they utilized a classification approach rather than the velocity vector prediction. In these studies, the imagined motion and the commanded robotic arm motion were not directly related. Therefore, it is hard to say that this control approach has solved the issues that arise in the conventional approaches.

Velocity control of a robotic arm based on EEG activated by motor imagery is a highly challenging purpose and has not yet exhibited satisfactory performance because of its limited spatial resolution and low signal-to-noise ratio [51]. It is a challenging goal that has been hard to achieve in the past, and it is difficult to expect to reach a practical level at once through this study. Thus, we focus on three further improvements that were not previously attempted.

In the first step, the velocity vector of hand movement is predicted. The PD based decoding model is not appropriate for EEG since its spatial resolution cannot reach the neuron level. Thus, a linear model for hand velocity prediction is considered, and the decoding power of the model is verified by predicting the real hand trajectory of a normal user. It has been shown that the motor imagery leads to the activation of similar brain areas as in actual movement [52]. Therefore, it is expected that the decoding model verified by real arm movement can be applied to decode motor imagery of patients with paralysis. Even though a previous study [53] estimated hand trajectory using EEG, the correlation between the real arm and predicted trajectories was not sufficiently high (mean correlation coefficient=0.19~0.38). Yeom et al. [54] proposed an improved approach by modifying the frequency band (0.5~8 Hz) because Rickert et al. [55] reported that the movement-evoked potential during arm movement includes components that are faster than 1 Hz. In the current study, the proposed approach was first applied to EEG, which is practical non-invasive neural signal. The hand trajectory of the reaching motion is predicted from the neural signals of a healthy subject. In addition, the robotic arm is driven based on the predicted trajectory. The control command for grasping motion is automatically given (pseudo-signal) at the closest position rather than derived from the neural signal. Furthermore, MEG and EEG are compared to consider the portability issue.

In the second step, a novel training system, which can improve motor imagery ability and decoding parameters, is proposed and developed. Even though the

shared control based training introduced in section 1.2.3 exhibited an effective training performance, it is limited to predetermined targets and tasks provided by training system. In this study, the previous algorithm is modified and additional functionality is added by using an RGB-D camera. Multiple targets can be detected and the positions are estimated automatically. Furthermore, the user intended target is selected automatically and the active shared control strategy attracts the robot end-effector to the intended target. Thus, the user can select which target to reach according to his or her own volition. When performing tasks reaching one of several targets, the chance level of reaching the correct target can be calculated as shown below because the active shared control algorithm eventually leads the robot end-effector to one of the targets and simply reaching the target point is not a measure of success.

$$\textit{Chance Level (\%)} = 100 \div \textit{Number of Targets} \quad (1.9)$$

In the final step, the developed training system is applied to two clinical cases of potential users (patients with cervical SCI) with functional magnetic resonance image (fMRI) studies to assess the feasibility and possible effects of the training. In total, 10 sessions of reaching imagery are performed of which the first 5 are performed with virtual reality (VR) videos so that the users are sufficiently familiar with the reaching behavior as the baseline. The next five sessions are performed using the developed BMI training system,

and the fMRI images are obtained before and after the application of the developed system. The flowchart in Fig. 1.7 represents the overall research flow.

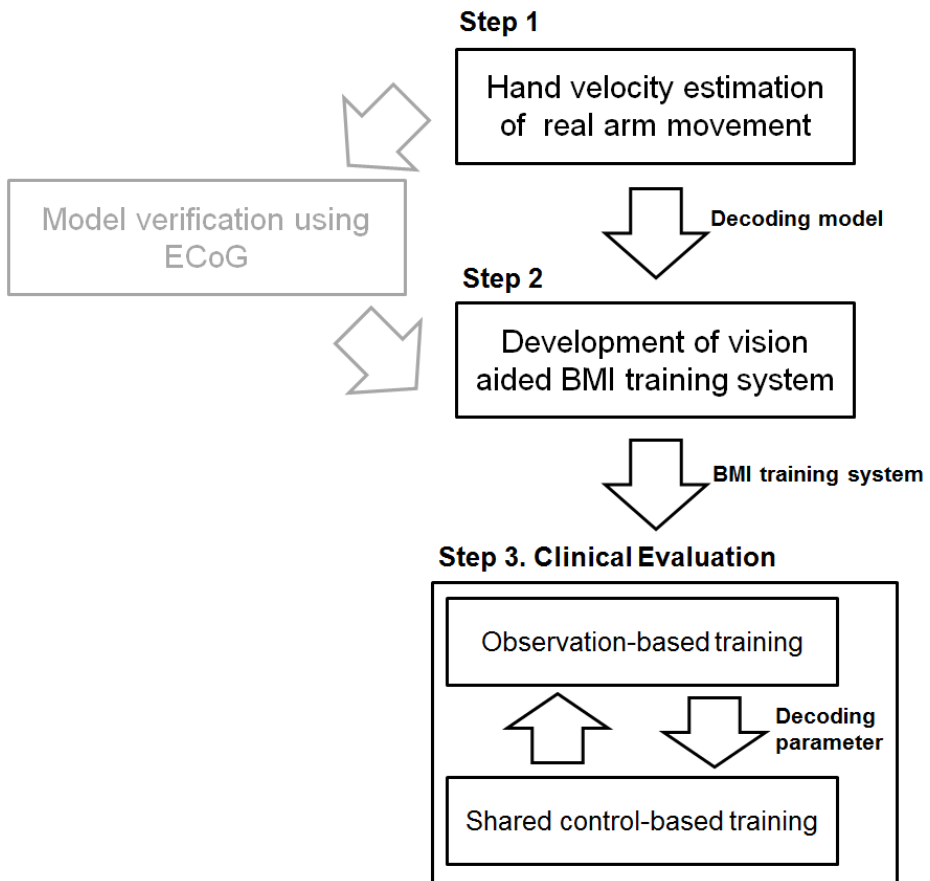


Fig. 1.7 Overall research flow. The current study consists of 3 steps. Model verification using ECoG is not treated because the invasive approach is not the focus of this study.

2. Materials and Methods

2.1. Hand Velocity Estimation of Real Arm Movement

2.1.1. Overview

In the first step of the study, linear decoder is used to estimate hand velocity of real arm movement. The signal processing procedure consists of signal acquisition, preprocessing, movement prediction, and coordinate transformation. Fig. 2.1 shows the signal processing procedure, which is explained in the following section. Furthermore, reaching and grasping (pseudo-signal) motions of robotic arm are conducted using predicted trajectory to mimic human reaching motion. Integrated robotic arm-gripper system (IRAGS) consisting of two industrial robots: a six-DOF robotic arm (VS-6556G, DENSO, Kariya, Aichi Prefecture, Japan) and an adaptive robotic gripper (three-finger adaptive gripper, Robotiq, Saint-Nicolas, QC, Canada) is used for the robotic motion.

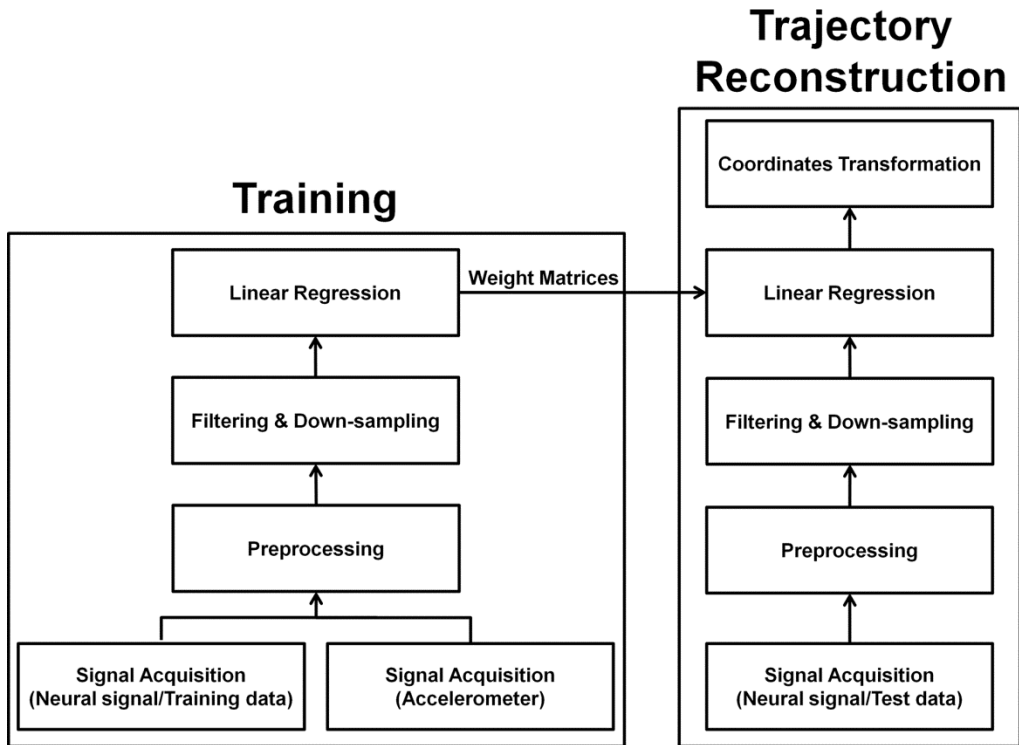


Fig. 2.1 Signal processing procedure. Training has to be conducted to obtain the weight matrices. The filtering, down-sampling, and linear regression processes are explained in the *Movement prediction* section.

2.1.2. Signal Acquisition and Processing

MEG

The acquisition of neural signals and the processing procedures are the same as those described in a previous study [54]. MEG signals are acquired from 306 channels of a whole-head MEG system (VectorView™, Elekta Neuromag Oy, Helsinki, Finland) in a magnetically shielded room. The 306 channels consist of 204 planar gradiometers and 102 magnetometers distributed at 102 locations. The sampling frequency is 600.615 Hz, and the signal is band-pass filtered in the range of 0.1~200 Hz. To eliminate external noise, the spatiotemporal signal space separation (tSSS) method is used. The neural signals are segmented from -1 s before the cue onset to 2 s after the cue onset and band-pass filtered in the range of 0.1~100 Hz. The 68 gradiometers of the 306 channels in the motor-related area are selected for movement prediction. The 68 gradiometers include motor-related areas [56] and demonstrate event-related desynchronization (ERD) around the alpha (8~13 Hz) and beta (13~30 Hz) frequencies [57]. An accelerometer (KXM52, Kionix, NY, USA) is placed on the index finger, and the sensor signals are simultaneously recorded with MEG at the same sampling rate.

EEG

EEG signals are measured by using a 64-channel EEG system (Synamps 2, Compumedics Neuroscan, Texas, USA). The sampling frequency is 1,000 Hz and low-pass filtered at 200 Hz. A notch filter is applied at 60 Hz to remove line noise. The signals are segmented from -1 s before the cue onset to 2 s after the cue onset. All 64 channels are used for movement prediction. Because the number of EEG channels is insufficient, in contrast to MEG, all channels are used to maximize accuracy even though they are distributed in not only the motor-related areas but also other areas. The accelerometer signals are simultaneously acquired with the EEG signals at the same sampling frequency.

Movement Prediction

The MEG and EEG signals are band-pass filtered in the range of 0.5~8 Hz. The accelerometer signals are filtered in the range of 0.2~5 Hz. The movement velocity is calculated by integrating the accelerometer signals with respect to time. The filtered neural signals are down-sampled at 50 Hz (20 ms intervals). The movement velocities are also down-sampled at 50 Hz (20 ms

intervals). Neural signals with 200 ms intervals (average of one current point and 10 preceding points) are used as features to predict the present velocity. The x , y , and z velocities of the movements are predicted from the neural signal by using multiple linear regressions. The regression equations are expressed below in equations (2.1)-(2.3).

$$V_x(t) = \sum_{i=1}^n \sum_{j=0}^m W_{ij}^x \times S_i(t-j) + W_0^x \quad (2.1)$$

$$V_y(t) = \sum_{i=1}^n \sum_{j=0}^m W_{ij}^y \times S_i(t-j) + W_0^y \quad (2.2)$$

$$V_z(t) = \sum_{i=1}^n \sum_{j=0}^m W_{ij}^z \times S_i(t-j) + W_0^z \quad (2.3)$$

$V_x(t)$, $V_y(t)$, and $V_z(t)$ are the calculated velocities from the accelerometer. W_{ij}^x , W_{ij}^y , and W_{ij}^z are the weight matrices, and S_i is the MEG/EEG signal of the i^{th} channel. n is the number of channels (68 for MEG and 64 for EEG), and m is the number of data points before the time t . The weight matrices are obtained first by training. Then, the weight matrices are used to predict the velocities from the neural signals. The trajectories are calculated by integrating the predicted velocities as given below in equations (2.4) and (2.5).

$$V(t) = [V_x(t) V_y(t) V_z(t)] \quad (2.4)$$

$$P(\tau) = \int_{t=0}^{\tau} V(t) dt \quad (2.5)$$

$V(t)$ is the predicted velocity vector at the time t , and $P(\tau)$ is the position vector at the time τ .

Coordinate Transformation

The coordinates of the IRAGS is defined as the reference frame, and the coordinates of the accelerometer is transformed into the IRAGS coordinates. It was assumed that the index finger is maintained at an angle of up to 30° from the horizontal plane. To maintain the angle between the index finger and horizontal plane at a constant value, the subjects were instructed to maintain their finger at the initial orientation. Although the invasive BMI studies achieved control of a robotic arm with seven-DOF (three-DOF translational motion, three-DOF orientational motion, and one-DOF grasping motion) [2, 23], the present study focused only on the three DOF of the translational movements. Therefore, the orientation of the index finger should be fixed to acquire the signal, which is not affected by the orientation movement of the hand. An additional method of controlling the orientation in future study is

discussed in the Discussion section. Coordinate transformation is performed by multiplying the rotational matrices. The rotation axis is defined as matrix A in equation (2.6), and the rotation matrix is represented as $R_A(\theta)$ in equation (2.7), where θ is the rotated angle. By multiplying the two rotation matrices as expressed in equation (2.8), the trajectory can be transformed from the accelerometer coordinates to the IRAGS coordinates. Fig. 2.2 shows the coordinates of each system and the trajectories before and after the transformation as an example.

$$A = [A_1 \quad A_2 \quad A_3] \quad (2.6)$$

$$R_A(\theta) = \begin{bmatrix} \cos\theta + (1 - \cos\theta)A_1^2 & (1 - \cos\theta)A_1A_2 - \sin\theta A_3 & (1 - \cos\theta)A_1A_3 + \sin\theta A_2 \\ (1 - \cos\theta)A_1A_2 + \sin\theta A_3 & \cos\theta + (1 - \cos\theta)A_2^2 & (1 - \cos\theta)A_2A_3 - \sin\theta A_1 \\ (1 - \cos\theta)A_1A_3 - \sin\theta A_2 & (1 - \cos\theta)A_2A_3 + \sin\theta A_1 & \cos\theta + (1 - \cos\theta)A_3^2 \end{bmatrix} \quad (2.7)$$

$$Coord_{robot} = R_y(-30^\circ) \cdot R_z(-90^\circ) \cdot Coord_{accelerometer} \quad (2.8)$$

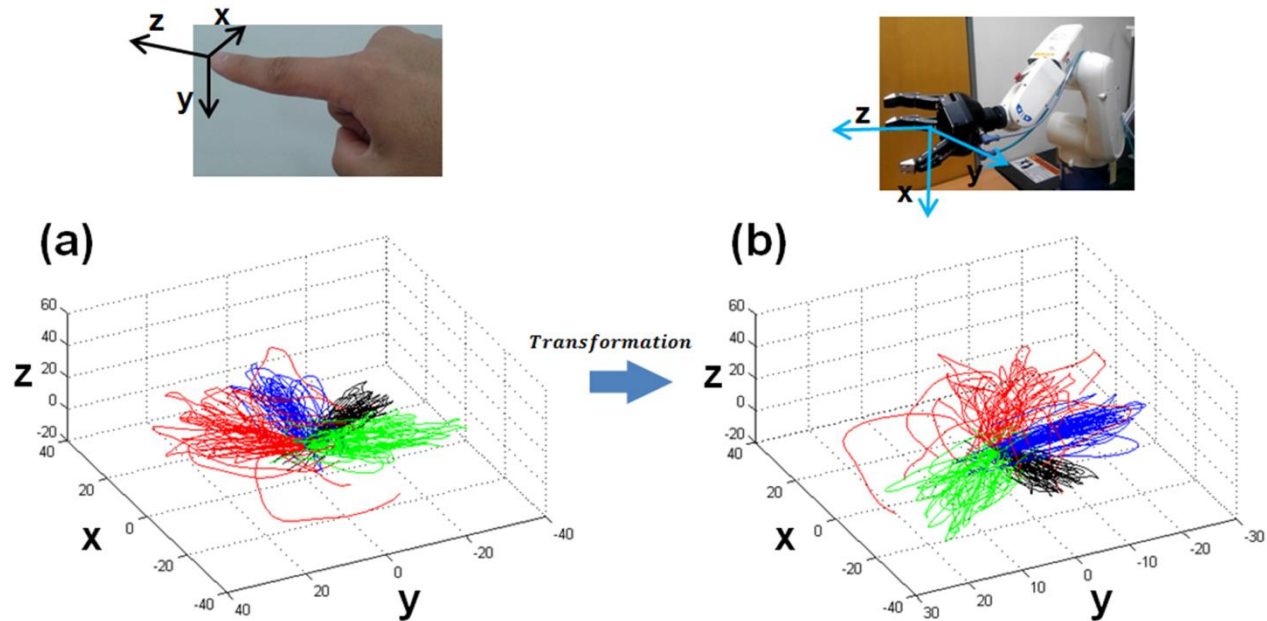


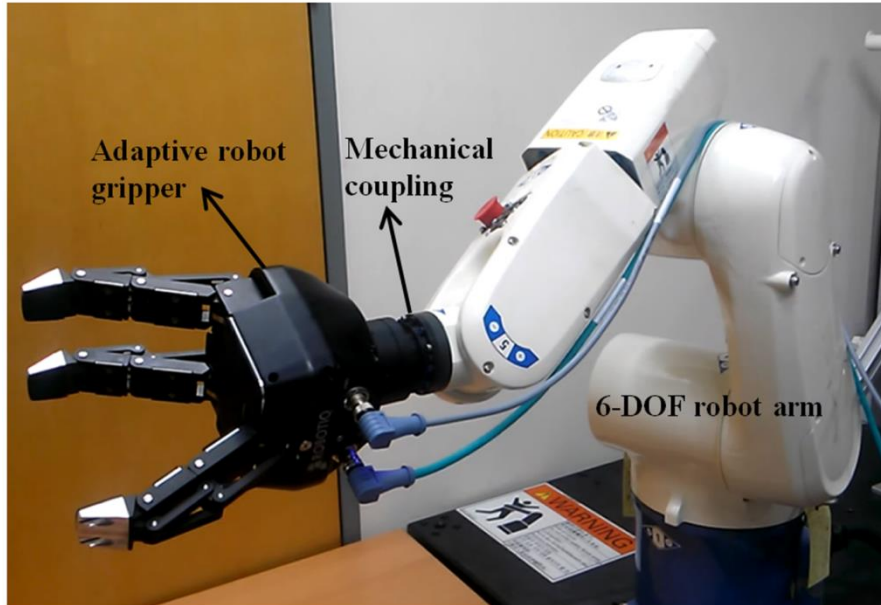
Fig. 2.2 Rotational transformation to change trajectories in the accelerometer coordinates to IRAGS coordinates. (a) Predicted hand trajectories reconstructed from neural signal before transformation. (b) Predicted hand trajectories after transformation. * Abbreviation: Integrated robotic arm-gripper system (IRAGS).

2.1.3. Robotic Arm Hardware

Six-DOF Robotic Arm

A six-DOF robotic arm movement consists of a translational movement and orientation rotation. The translational movement is predicted by neural signals, whereas the orientation rotation is assigned to maintain the end-effector in the horizontal direction. Therefore, the six-DOF robotic arm is controlled with three-DOF translational motion. In a recent study, Bennis and Roby-Brami found that the orientation of the human hand is closely related to its velocity vector [58]. However, the orientation is not that significant when the object has a spherical shape, and a spherically shaped object was used for grasping in this study. The robotic arm is controlled by an algorithm based on Microsoft Visual Studio 2010 (Microsoft, Redmond, WA, USA). The six-DOF robotic arm contains an external controller, and it communicates by using a personal computer through a binary controller access protocol. The six-DOF robotic arm is shown in Fig. 2.3.

(a)



(b)

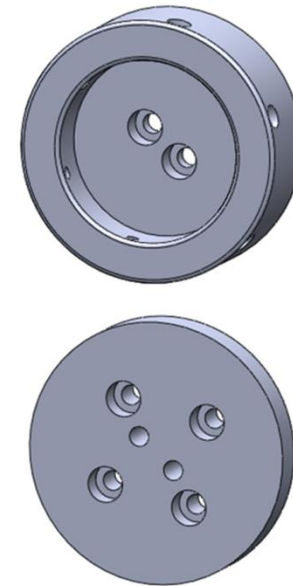


Fig. 2.3 Integrated robotic arm-gripper system (IRAGS). (a) Hardware of the IRAGS. The IRAGS consists of a six-DOF robotic arm, adaptive robotic gripper, and mechanical coupling. (b) Mechanical coupling to connect the six-DOF robotic arm and adaptive robotic gripper.

Adaptive Robotic Gripper

The industrial adaptive gripper is an optimized machine for grasping. The adaptive robotic gripper consists of three fingers and has five DOF. Three of the five DOF are used for the grasping motion, and the others are used for the lateral motion of two fingers. The five DOF are coupled to a single-DOF motion to grasp a spherical object based upon a simple command. A controller is installed inside the robot. The transmission control protocol and internet protocol are used for communication. The control algorithm is implemented with MATLAB[®] R2013b (MathWorks, Natick, MA, USA). The maximum grasping force and speed are set to 15N and 22mm/s, respectively. The internal controller stops the grasping motion when each finger reaches the assigned maximum grasping force. Power is supplied from a regulated direct-current power supply (PWS-3005D, Provice, Hwaseong-si, Gyeonggi-do, Korea) and the voltage is set to 24V. The adaptive robotic gripper is shown in Fig. 2.3(a).

Robot System Integration

To integrate the robotic arm and gripper, a mechanical coupling was designed. The implemented IRAGS and mechanical coupling are shown in Fig. 2.3(a) and (b), respectively. The robotic arm is controlled by an algorithm based on Microsoft Visual Studio, and the adaptive robotic gripper is controlled by an algorithm based on MATLAB[®]. To control the IRAGS with a single algorithm, the system is implemented so that the robotic arm and gripper can interact. If a grasping signal is provided to the IRAGS, the adaptive robotic gripper performs a grasping motion, while the robotic arm stops moving. The IRAGS is controlled with four DOF. Three DOF are for the translational movement of the six-DOF robotic arm, and one DOF is for the grasping motion of the adaptive robotic gripper.

2.1.4. Performance Verification

The prediction model was used for operation of IRAGS. The success rate of the reaching and grasping motions with the IRAGS was measured to predict whether the system can be acceptable in real-world situations. The input was provided off-line.

As the first step, MEG and EEG signals were acquired, and the trajectories of the human arm movement were predicted. The neural activity was measured during the reaching movements with MEG and EEG. Nine healthy subjects for each signal (MEG case: 19–37 years old, five males and four females; EEG case: 25~31 years old, five males and four females) participated in the study. Stereographic images were presented to the subjects to guide the reaching movements. At the start of the experiment, an image of a sphere was presented at the center of a screen, and each subject was instructed to put his/her index finger on the sphere. After 4 s, a target sphere appeared randomly at each of the four corners of the screen. The subject was instructed to move the index finger to the target sphere and then move it back to the center. These reaching movements were repeated during the experiments. Two sessions were performed by each subject. For each session, the subjects performed reaching movements for 30 trials in each direction. The experiment was approved by the Institutional Review Board (IRB) of Seoul National University Hospital (IRB No.: 1501-006-637). The trajectories were predicted

by five-fold cross validation. This method separates four-fifths of the data for training (obtaining weight matrices) and one-fifth for testing. Thus, five combinations of training and testing data were available. Through the validation, test data was obtained. The method of cross validation has been used in previous studies to obtain generalizability [53, 54]. The process of five-fold cross validation for predicting 3D hand trajectory is demonstrated in Fig. 2.4. The length of the trajectories reconstructed by integrating the accelerometer signal was scaled to 30 cm by multiplying the scaling coefficient. The scaling coefficient was used to scale the reconstructed trajectories derived from the neural signal.

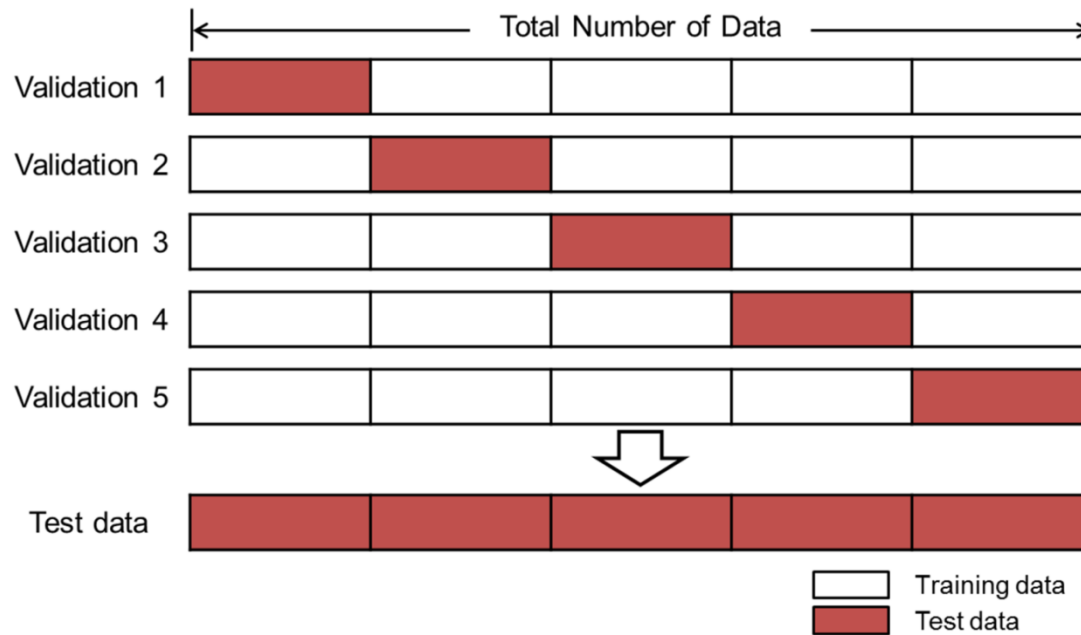


Fig 2.4 Five-fold cross validation for hand trajectory prediction. In the five-fold cross validation process, the test data, which guarantee generalizability, is obtained.

As the second step, the position of the target object was defined. A plastic sphere was fixed at a position as a target. To define the position of the target object, information from a real-limb trajectory was used. Even though no real plastic sphere existed when the neural signal was acquired, the subjects felt their fingers reached the target object (the stereographic images) when their arms were completely stretched. Therefore, we fixed the target object at the average of the terminal positions of the real trajectories. By using the accelerometer data, the average of the real terminal positions in each direction (four directions) and in each session (18 sessions) was calculated. The values of the x , y , and z coordinates were averaged, as expressed in equations (2.9)-(2.11).

$$x_{avg} = \frac{1}{30} \sum_{i=1}^{30} x_{term,i} \quad (2.9)$$

$$y_{avg} = \frac{1}{30} \sum_{i=1}^{30} y_{term,i} \quad (2.10)$$

$$z_{avg} = \frac{1}{30} \sum_{i=1}^{30} z_{term,i} \quad (2.11)$$

$[x_{avg} \ y_{avg} \ z_{avg}]$ is the calculated position to fix the target object, and $[x_{term,i} \ y_{term,i} \ z_{term,i}]$ is the terminal position of the i_{th} trajectory in each

session. The diameter of the target sphere was 70mm, which is approximately the size of a baseball (a baseball has a circumference of approximately 23cm, for a diameter of approximately 73mm) and is a comfortable size for grasping by an average person.

As the final step, IRAGS was used to perform reaching and grasping motions. To dexterously perform reaching and grasping motions, seven DOF are necessary (three for translational movement, three for orientation, and one for grasping) [59]. Only the three DOF of the translational movement were predicted in the present study, and the three DOF of the orientation were fixed as constant. A pseudo-grasping signal was provided for the grasping motion. The pseudo-grasping signal was automatically provided when the distance between the adaptive robotic gripper and target sphere was at its shortest.

The accuracy of the predicted trajectories was evaluated by calculating the correlation coefficient, root mean square error (RMSE) and terminal point error (TPE). TPE indicates the distance from trajectory to target surface at the closest position. The grasping and touching target success rates were also measured.

2.2. Development of Vision-Aided Training System

2.2.1. System Overview

Shared control based BMI trainings for multi-DOF robotic arm control has been conducted for improved decoding parameter acquisition and user adaptation of motor imagery. Even though previous shared control strategies were highly effective, they are limited to preprogrammed target. In the current study, further improvements are added for user to select target by their own. The proposed training system automatically detects the target object on the basis of the image and uses the image information as well as the brain signal information for easier control of the robotic arm. Kinect is used for image acquisition, and separation of pixel color and hierarchical clustering is applied for detection of multiple target objects. Active shared control is applied rather than passive type by considering limited performance of EEG based decoding. As the dependency of image information is higher rather than that of brain signal information, the difficulty of robotic arm control is lowered. Further specific details are described in sections below. The overall flow of the proposed BMI training system is represented in Fig. 2.5.

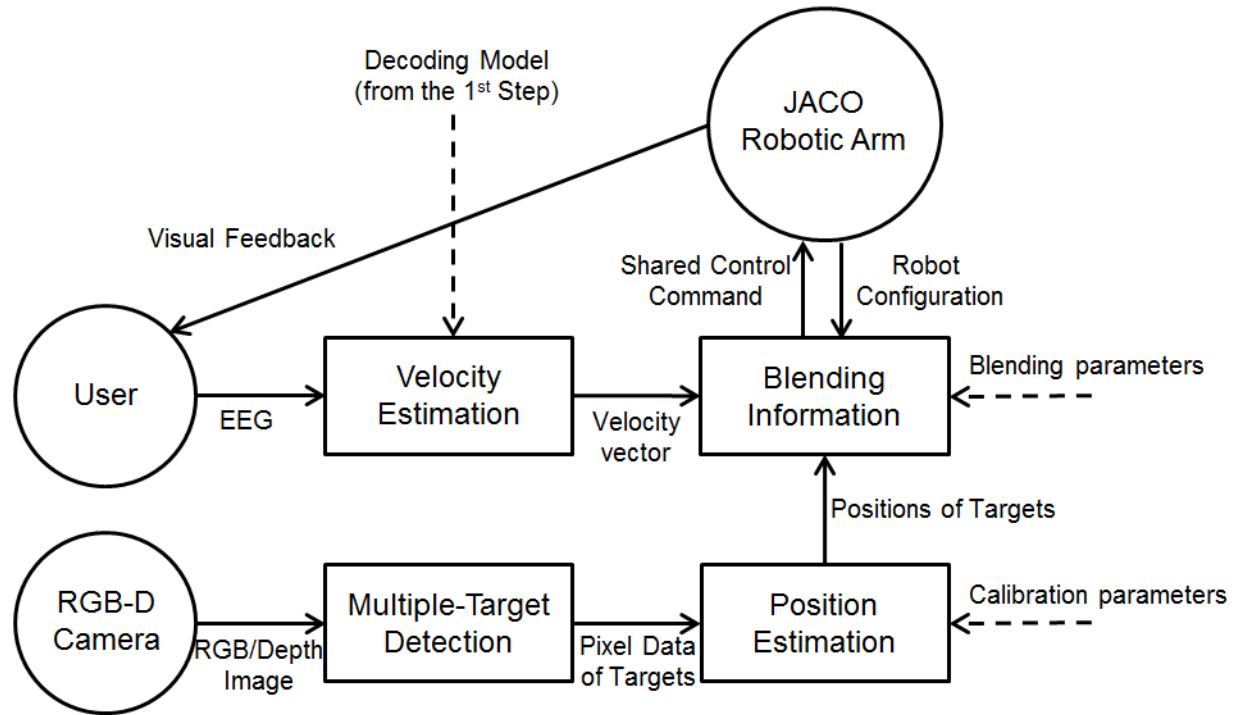


Fig 2.5 Overall flow of the proposed BMI training system. The solid line represents the flow of the signal, and the dotted line represents the model and parameters used.

2.2.2. Target Object Detection and Camera Calibration

Target Object Detection Using the Kinect

The position of target objects must be accurately defined to compensate the predicted hand trajectory from neural signals. Before their position can be estimated, the targets must be detected. Although various target detection algorithms have been reported, elaborate algorithms are not required for the BMI training system because it is operated in a relatively well-arranged space with clean background. Green balls (diameter: 7 cm) serve as targets in this study, so binary images (green: 1; else: 0) were acquired using RGB images obtained by the Kinect (Kinect for XBOX 360, Microsoft, Redmond, WA, US). Using RGB values from the image, green pixels were separated, as shown in Equation (2.12).

$$\frac{G}{R + G + B} > 0.5 \quad (2.12)$$

The images were filtered to remove noise via the process described in Equations (2.13) and (2.14).

$$Average(i, j) = \frac{1}{9} \sum_{k=-1}^1 \sum_{l=-1}^1 index(i + k, j + l) \quad (2.13)$$

$$Filtered\ pixel(i, j) = \begin{cases} 1 & \text{if } Average(i, j) = 1 \\ 0 & \text{otherwise} \end{cases} \quad (2.14)$$

Noise-filtered images can contain more than one target object, so pixels designated as “1” should be clustered to their corresponding target object. Hierarchical clustering distinguishes multiple target objects simultaneously. Conventional clustering algorithms require the number of clusters to be predetermined for centroid generation. However, a BMI system is highly limited if the number of target object is predetermined; thus, a divisive hierarchical clustering approach was chosen instead. This approach initially assumes that there is one target object is. When the x or y axis standard deviation of pixels are equal or larger than 20, the cluster is reclustered with two centroids. This procedure is repeated until all clusters have a pixel distribution whose standard deviation is less than 20 in both the x and y axes. The target detection procedure is summarized in Fig. 2.6.

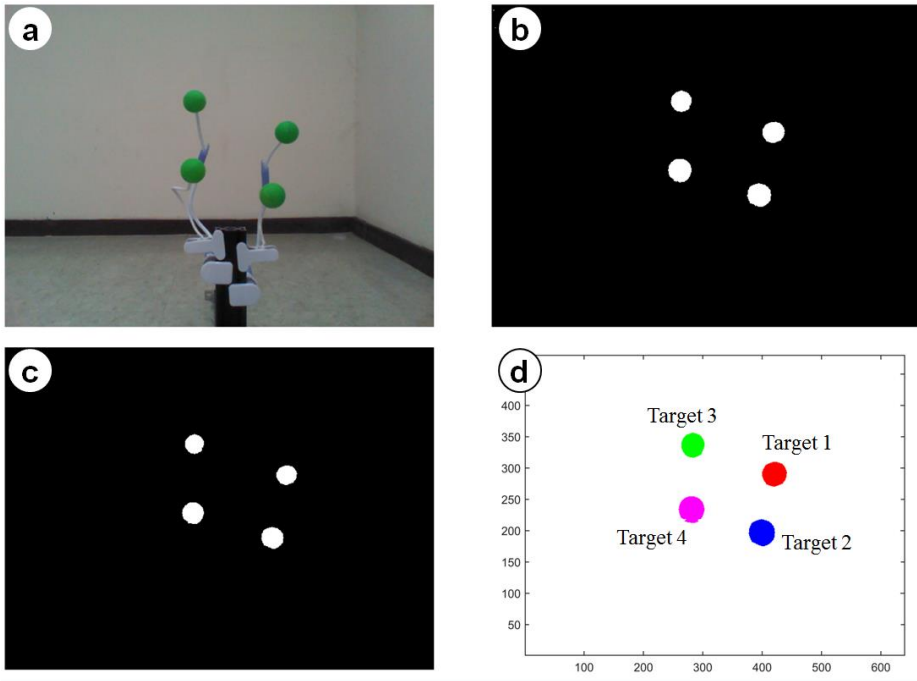


Fig. 2.6 Procedure for target object detection. (a) RGB image obtained from Kinect. (b) Binary image. (c) Noise-filtered image. (d) Object detection via hierarchical clustering.

To validate the algorithm, an environment containing several green target objects was prepared and photographed with the Kinect. The number of target objects ranged from two to four and 20 images were acquired for each number of target objects (for a total of 60 images). The distance between target objects was controlled within the range from 15 cm to 35 cm. For each number of target objects, the accuracy of detecting all existing targets was measured.

Camera Calibration

The 3D position of detected target object should be estimated using information acquired from images. The Kinect provides two types of images: RGB and depth images. RGB images provide three channels of data with 480×640 resolution. Depth images provide one channel of 480×640 resolution; each pixel represents a depth index related to the distance to objects in the image. Using three types of camera calibration, the 3D position of each target object can be estimated.

The first calibration consists of distortion compensation between the RGB and depth images. The same object is reflected in different pixels in the RGB and depth images, so calibration to match the two images is necessary for position estimation (Fig. 2.7(a)). Linear regression was applied to obtain the transformation matrix for the mapping. Images with several balls were

photographed with the RGB and depth camera, respectively (Fig. 2.7(b)), and the pixel coordinates of the balls were measured. This process was repeated to obtain a larger dataset. The coordinates of the balls from the RGB images were stored to matrix A with a size of 165×2 , which contains pixel information of 165 balls. Matrix D , for the depth image, was obtained similarly. Then, matrix B , which maps pixels from the RGB to the depth image, can be obtained with the linear regression in equations (2.15) and (2.16).

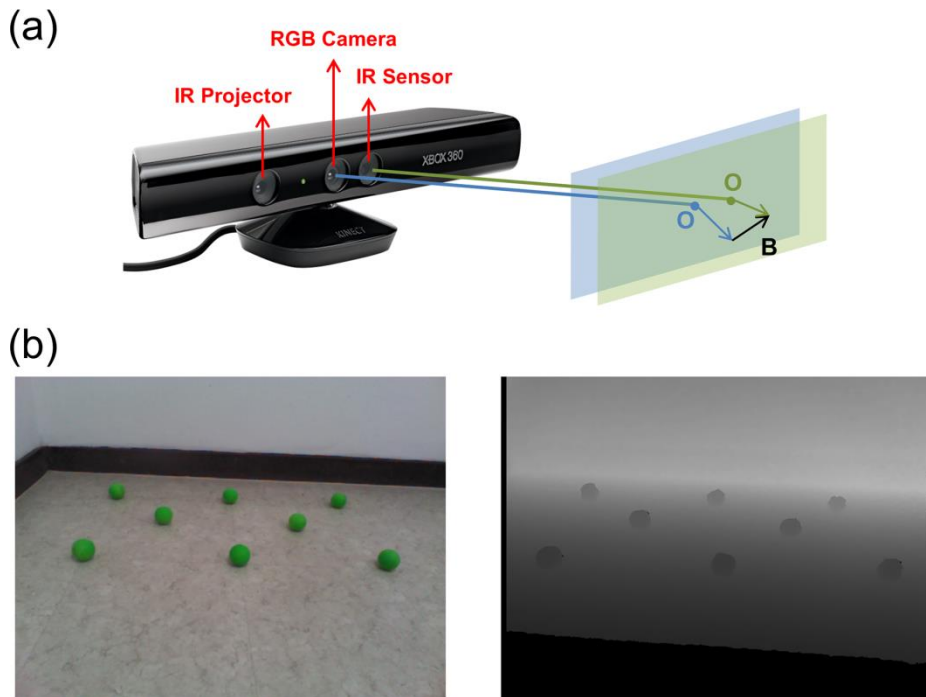


Fig. 2.7 (a) Distortion between RGB and depth images caused by location of the sensors. (b) The same image photographed by the RGB (left) and depth (right) cameras, respectively.

$$D = [A \ 1] \times B \quad (2.15)$$

$$B = (X^T X)^{-1} X^T D, \quad X = [A \ 1] \quad (2.16)$$

Thus, B was obtained as shown below. The R^2 values for the x - and y -axes were nearly 1.0 (> 0.999) and their root mean square errors (RMSEs) were 2.97 and 2.40 pixels, respectively. This result indicates that less than 3 pixels of error are occurred with the proposed linear regression. When total size of the images (480×640 pixels) is considered, this error seems to be trivial.

$$B = \begin{bmatrix} 1.17332 & 0.000815 \\ -0.01963 & 1.12255 \\ -34.6797 & -20.0941 \end{bmatrix} \quad (2.17)$$

The second calibration was conducted between the depth index and real distance (Fig. 2.8(a)). A linear fitting provided by the MATLAB[®] Curve Fitting Toolbox (MATLAB[®] R2016b, Mathworks Inc., Natick, MA, US) was utilized, and the result is shown in equation (2.18). *dist.* indicates the real distance and R^2 value of the linear fitting is 0.9987.

$$dist. (m) = 61.5 \times Depth\ index + 0.1046 \quad (2.18)$$

Finally, 2D position was estimated from the x and y pixels of the RGB image. To estimate x and y coordinates, distance and number of pixels in x and y axes from the center of image were used (Fig. 2.8(b)). Two points with distance $l = 30\text{cm}$ on wall were repeatedly photographed with RGB camera of Kinect and the x and y axes distances were estimated using the following linear models.

$$l^2 = [a^2 \quad b^2] \begin{bmatrix} \text{Pixel}_x^2 \\ \text{Pixel}_y^2 \end{bmatrix} \quad (2.19)$$

$$x(m) = a \times \text{Pixel}_x \quad (2.20)$$

$$y(m) = b \times \text{Pixel}_y \quad (2.21)$$

$$a = a_1 \times \text{dist. (m)} + a_2 \quad (2.22)$$

$$b = b_1 \times \text{dist. (m)} + b_2 \quad (2.23)$$

Based on linear fitting, the results below were derived. R^2 values for x and y axes are 0.9939 and 0.9784 respectively. The center of the RGB image was defined as the origin.

$$x(m) = (0.001937 \times \text{dist. (m)} + 0.0001662) \times \text{Pixel}_x \quad (2.24)$$

$$y(m) = (0.002072 \times \text{dist.}(m) - 0.000227) \times \text{Pixel}_y \quad (2.25)$$

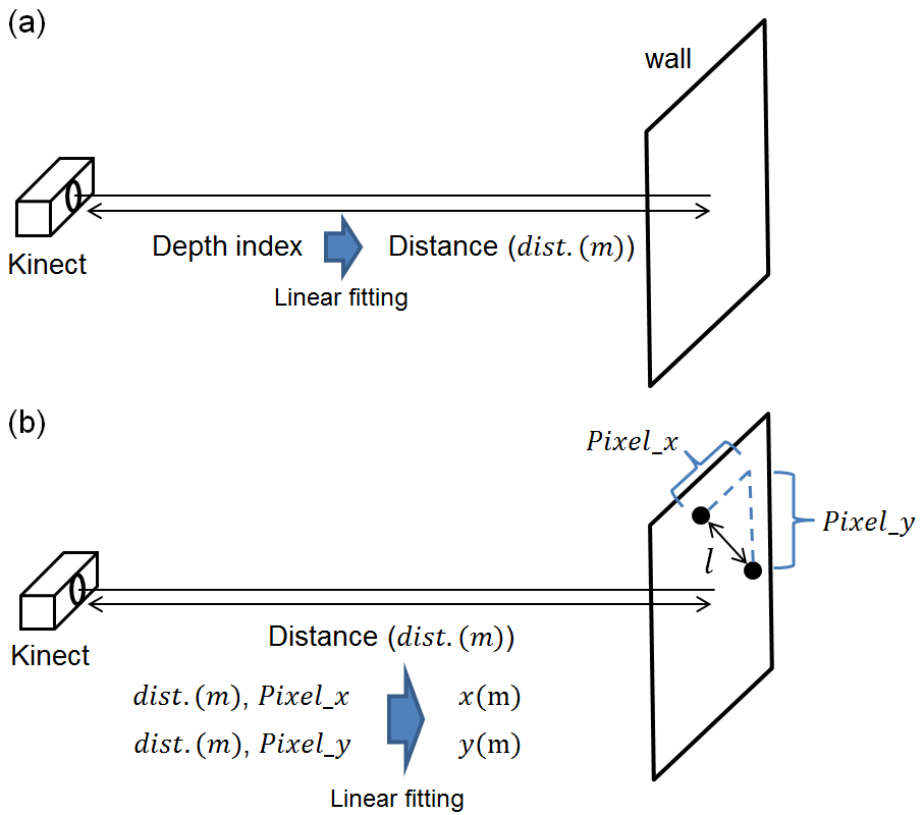


Fig. 2.8 (a) calibration for distance estimation. (b) calibration for *x* and *y* coordinates estimation.

To validate the implemented algorithm, it was compared with an optic tracker (PST Base, ps-tech, Amsterdam, Netherlands) that estimates the 3D position of pre-attached stickers with high accuracy (position < 0.5 mm RMSE, orientation $< 1^\circ$ RMSE²). Two target objects with pre-attached stickers were prepared and placed randomly on the prepared experimental setup, as depicted in Fig. 2.9. The distance between the two target objects was measured using the optic tracker and Kinect. This procedure was repeated 10 times and the difference between the two approaches was analyzed.

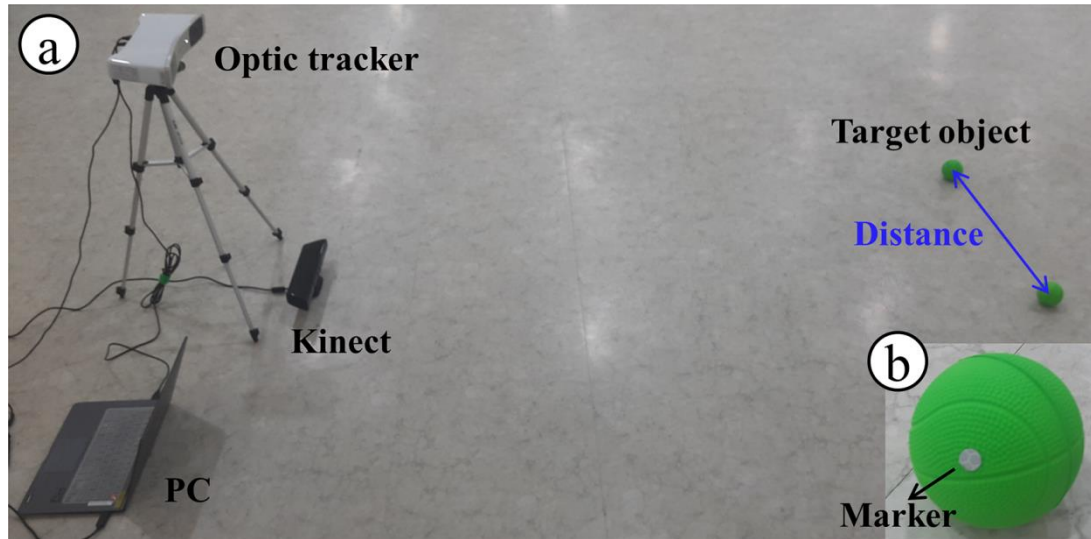


Fig. 2.9 Experimental setup to validate camera calibration for position estimation.

2.2.3. Training System Hardware

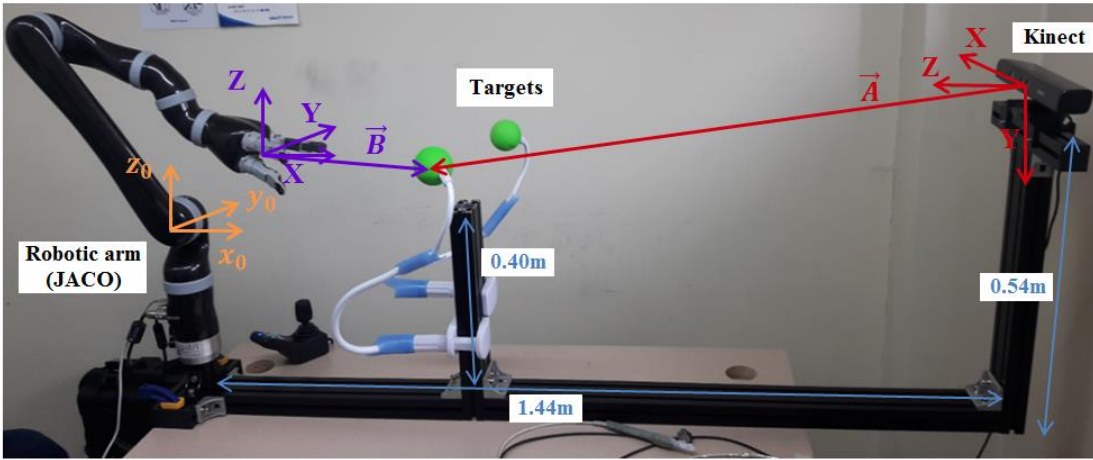
The vision-aided BMI training system consists of three components: a six-DOF anthropomorphic robotic arm (JACO, Kinova, Boisbriand, QC, Canada), Kinect, and targets. Aluminum profiles are fixing the components. The dimensions of the aluminum profiles were designed by considering the workspace of the robotic arm, as shown in Fig. 2.10(a). The arm was fixed on one side of the aluminum profiles and the Kinect on the other. The green target objects were fixed between them using flexible supports. Kinect detects target objects and the estimated positions are delivered to the robotic arm for its waypoint generation. The coordinates of the Kinect and robotic arm are different; thus, the homogeneous transformation matrix (equations (2.26) and (2.27)) should be multiplied before the target position vector for waypoint generation.

$$\begin{bmatrix} \vec{B} \\ 1 \end{bmatrix} = T \begin{bmatrix} \vec{A} \\ 1 \end{bmatrix} \quad (2.26)$$

$$T = \begin{bmatrix} R & 1.24 \\ 0 & 0 & 0 & 0 \\ 0 & 0 & 0 & 1 \end{bmatrix}, \quad (R = \begin{bmatrix} 0 & 0 & -1 \\ 1 & 0 & 0 \\ 0 & -1 & 0 \end{bmatrix}) \quad (2.27)$$

Vectors \vec{A} and \vec{B} are the position of target object measured from the Kinect and robotic gripper, respectively. The origin of the robotic arm was defined as a point with an offset of 0.2 m in the x and z axes from the origin of frame 0 (the center of joint 2, see Fig. 2.10(a)).

(a)



(b)

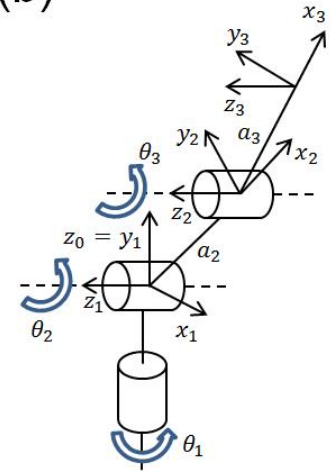


Fig. 2.10 (a) BMI training system, consisting of a robotic arm, Kinect, and targets. (b) Frames and variables of the robotic arm kinematics.

2.2.4. Shared Control Strategy

To generate shared control based waypoints of robot operation, both the neural signals and the target object location should be considered. Previous studies reported shared control, which blended a predicted velocity vector and the ideal vector to a preprogrammed target object; however, to the best of our knowledge, none have considered a situation that includes more than one target object with no preprogrammed information. Thus, it is necessary to propose a novel shared control strategy for a BMI system that is applicable to situations with multiple targets. To solve this issue, our research utilized artificial potential, which is a conventional motion planning approach for robots to avoid obstacles and reach destinations. The conventional approaches were modified into a proper form to be applied to the BMI training system. This attracts the robots to the most probable target object that allows the robot end-effector to approach the user-intended target. The joints of the robotic arm are compensated for by blending the predicted hand velocity and the ideal vector to the intended target.

The detailed algorithm for shared control is described below. First, artificial potential was formed by considering multiple target objects using equations (2.28)–(2.30).

$$e_i = q_{g,i} - q \quad (i = 1, 2, 3, \dots, \text{Number of target objects}) \quad (2.28)$$

$$U_{a,i} = \frac{1}{2} k_{a,i} e_i^T(q) e_i(q) \quad (2.29)$$

$$f_t = \sum_{i=1}^4 f_{a,i} \quad (f_{a,i} = k_{a,i} e_i(q)) \quad (2.30)$$

q is the configuration of the joints and $q_{g,i}$ is the goal configuration for the i^{th} target object. $U_{a,i}$ is the artificial potential provided by the i^{th} target object. The stiffness $k_{a,i}$ is programmed to be equal to 1 when the user of the BMI system intends to reach the i^{th} target object. The intended target object is determined by the currently predicted velocity from the neural signals. The angle between the predicted velocity vector and the vector from the current position to each target position is calculated and the target with the smallest angle is determined to be the intended target object. For the unselected target objects, $k_{a,i}$ is set to 0. So, f_t is the attractive force acted by an intended target. The attractive force f_t increases as the error of the robotic configuration to the intended target object increases. The intended target object is updated for each stage of waypoint generation. Thus, the BMI user can change the preferred target object while controlling the robotic arm. Then, the ideal vector to the intended target object is generated based on the current waypoint of the end-effector and the attractive force f_t as shown in equation (2.31).

$$\Delta x_{i,k} = x_e(q_k + f_t(q_k)) - x_e(q_k) \quad (2.31)$$

$x_e(q_k)$ is the k^{th} waypoint for the robotic arm end-effector and the vector $\Delta x_{i,k}$ points to the ideal direction to approach the intended target. When the predicted hand velocity vector moves away from the origin and the angle to the most intended target object is less than 90° , the next waypoint is generated via equations (2.32) and (2.33). Otherwise, the predicted velocity is not compensated.

$$\Delta x_k = 1.5 \left\{ \alpha \left(\Delta x_{i,k} \frac{\|\Delta x_{n,k}\|}{\|\Delta x_{i,k}\|} \right) + (1 - \alpha) \Delta x_{n,k} \right\} \quad (2.32)$$

$$x_e(q_{k+1}) = x_e(q_k) + \beta \Delta x_{k+1} + (1 - \beta) \Delta x_k \quad (2.33)$$

Δx_k is the compensation vector for the k^{th} waypoint and $\Delta x_{n,k}$ is the hand velocity vector predicted from neural signals. The vector $\Delta x_{i,k}$, which points in the ideal direction to the intended target, is scaled to the size of vector $\Delta x_{n,k}$, and the two vectors are blended with the proportions of α and $1 - \alpha$. The larger α increases the compensation from the Kinect and decreases the strength of the hand velocity originally predicted from the neural signals. Additionally, inertia is considered via parameter β to suppress any unintended sudden movement of the robotic arm. Similar BMI studies on

shared control also considered the issue of reducing acceleration, applying a smoothing approach to motion planning [60]. In equation (2.33), the compensation for the $k + 1^{th}$ waypoint is provided by blending the k^{th} compensation vector with the proportion of $1 - \beta$. Blending parameters α and β both range from 0 to 1.

To calculate the equations of the proposed shared control strategy, forward and inverse kinematics of the robotic arm are required; conventional kinematics of a three-DOF anthropomorphic arm [59] were utilized in the current study. The homogeneous transformation matrix for forward kinematics is suggested in equation (2.34). The Denavit–Hartenberg parameters for deriving the matrix are listed in Table 2.1.

$$T_{forward}(q) = \begin{bmatrix} c_1 c_{23} & -c_1 s_{23} & s_1 & c_1(a_2 c_2 + a_3 c_{23}) \\ s_1 c_{23} & -s_1 s_{23} & -c_1 & s_1(a_2 c_2 + a_3 c_{23}) \\ s_{23} & c_{23} & 0 & a_2 s_2 + a_3 s_{23} \\ 0 & 0 & 0 & 1 \end{bmatrix} \quad (2.34)$$

Relevant nomenclature is suggested in Fig. 2.10(b). c_1 , c_2 , and c_3 indicate $\cos\theta_1$, $\cos\theta_2$, and $\cos\theta_3$. s_1 , s_2 , and s_3 indicate $\sin\theta_1$, $\sin\theta_2$, and $\sin\theta_3$. Furthermore, c_{23} and s_{23} indicate $\cos(\theta_2 + \theta_3)$ and $\sin(\theta_2 + \theta_3)$, respectively. Additional information for the inverse kinematics is suggested in equations (2.35)–(2.37).

$$\theta_3 = \text{atan2}(s_3, c_3) \quad (2.35)$$

$$\theta_2 = \text{atan2}((a_2 + a_3 c_3)pW_z - a_3 s_3 \sqrt{pW_x^2 + pW_y^2},$$

$$(a_2 + a_3 c_3) \sqrt{pW_x^2 + pW_y^2} + a_3 s_3 pW_z) \quad (2.36)$$

$$\theta_1 = \text{atan2}(pW_y, pW_x) \quad (2.37)$$

pW_x , pW_y , and pW_z indicate the x , y , and z coordinates of the end-effector position measured in frame 0.

The shared control algorithm was applied to hand trajectories predicted from the EEG signals. Recorded predicted hand trajectories obtained in previous research [51] were used. The dataset contains 120 hand trajectories predicted from a healthy subject consisting of 4 directional reaching movements (30 trials per direction). Blending parameters α and β affect the performance of the algorithm and were modulated from 0.05 to 1.00 in intervals of 0.05 for optimization.

Table 2.1 Denavit-Hartenberg parameters for the robotic arm

Link	a_i	α_i	d_i	θ_i
1	0	$\pi/2$	0	θ_1
2	$a_2 = 0.41m$	0	0	θ_2
3	$a_3 = 0.44m$	0	0	θ_3

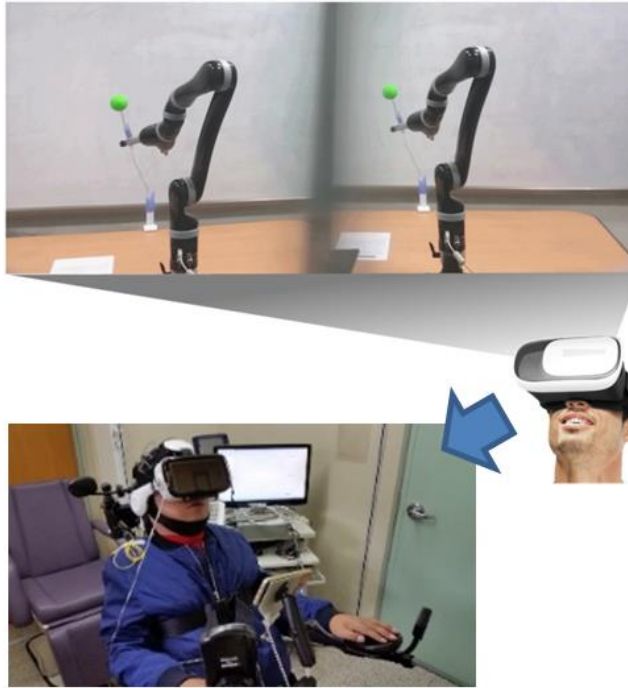
2.3. Clinical Application and fMRI Evaluation

Clinical Application

Developed BMI training system was clinically applied to patients with upper limb paralysis. Two volunteers with severe upper limb impairment due to cervical SCI participated in this study. Subject #1 is a 31-year-old male with American Spinal Injury Association Impairment Scale (AIS) C at level C4, and subject #2 is a 47-year-old male with AIS B at level C4. These patients are completely unable to control their own arms. The subjects were given a total of 10 sessions for training. The first 5 sessions were designed to help the subjects get used to motor imagery using targets and VR video files (Fig. 2.11(a)). In the next 5 sessions, developed BMI training system was utilized (Fig. 2.11(b)). Two types of training were conducted in each session. As the first type, observation-based training was performed and the parameters of the decoder were determined using multiple linear regressions between robotic arm motion and EEG signal. Since the decoder was not yet verified by patients with upper limb paralysis, blending parameters were set to high value. After observation-based training of each session, shared control based robotic arm control was attempted with blending parameters $\alpha = \beta = 0.6$. For each trial of shared control session, users were instructed to choose one target out

of two and success rate was measured for about 40 trials. fMRI while performing motor imagery tasks was taken before the 6th training session and after the 10th training session. Overall plan of clinical application is represented in Fig. 2.12. This clinical study was approved by the Institutional Review Board of Seoul National University Hospital (IRB No. 1605-136-765).

(a) Virtual reality based training



(b) Observation-based training ($\alpha = 1$) /
Shared control trial ($\alpha < 1$)

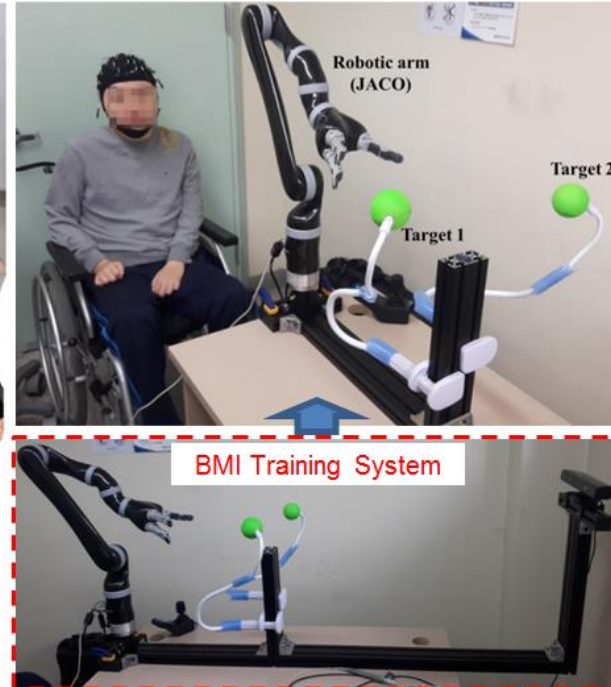


Fig. 2.11 Training setup. (a) Virtual reality based training for the first 5 sessions. (b) Observation-based training for the last 5 sessions. After each observation-based training, shared control based reaching target was attempted to confirm improved decoding performance.

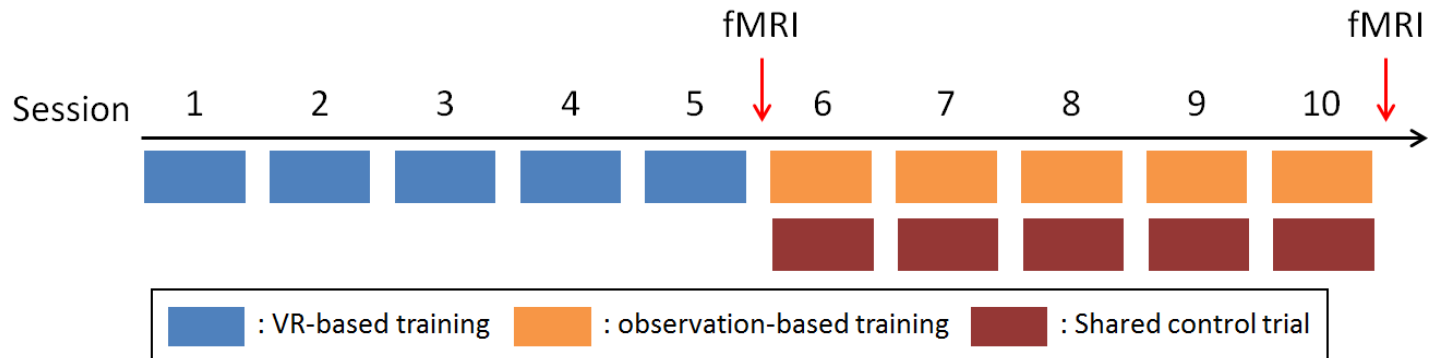


Fig. 2.12 Overall plan of clinical application.

fMRI Evaluation

Functional imaging consisted of motor imagery tasks in 3 directions: upper, lower-left, and lower-right. Block design was used in all tasks; during each task, subjects were instructed to imagine reaching and grasping movements repeatedly in selected directions. For each task, 8 active blocks and 7 rest blocks (each 20 seconds) were interleaved. The fMRI images were acquired with a Siemens MAGNETOM Trio, A Tim Syngo scanner using echo planar imaging (EPI, TE = 30 ms, TR = 3,000 ms), angulated in parallel to the anterior and posterior commissure line. A T1-weighted image was also obtained for anatomical reference. The fMRI data were preprocessed using Statistical Parametric Mapping 12 (SPM12, Wellcome Trust Centre for Neuroimaging, London, UK; www.fil.ion.ucl.ac.uk/spm/) executed in MATLAB® 2015b (Mathworks Inc., Natick, MA).

3. Results

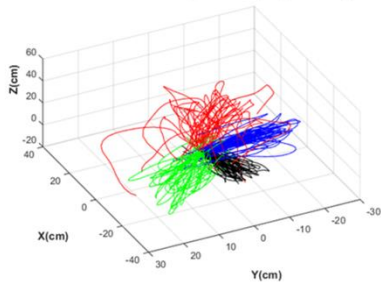
3.1. Performance of Hand Trajectory Prediction

Accuracy of the Predicted Trajectory

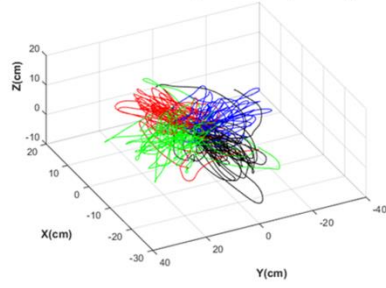
MEG was measured for two sessions from each of the nine subjects. Each session consisted of 120 trials. In total, 2,160 trials were conducted with MEG. As an example, Fig. 3.1(a) shows the predicted trajectories from the first session of subject 4. Fig. 3.1(b) shows the real trajectories derived from the accelerometer. The correlation coefficient, RMSE, and TPE were measured to evaluate the accuracies of the predicted trajectories. These are listed in Table 3.1. The average correlation coefficients from each session were significant ($p \cong 0.027$ for the least accurate session). The total correlation coefficient between the real and predicted trajectories was 0.705 ± 0.292 ($p < 0.001$) on average. The data from subject 2 exhibited a low correlation coefficient because the reaching behavior of the subject during the task was inconsistent. RMSE is an index that indicates the average Euclidean distance between the real and predicted trajectories. The average RMSE was 11.154 ± 5.399 cm. Except for three sessions (one session contained an outlier, and the other two

sessions were from subject 2 who exhibited inconsistent reaching behavior was performed), all other sessions exhibited an RMSE of less than 12 cm. TPE indicates the distance between the surface of the target sphere and the predicted trajectory at the closest position. The average TPE was 9.714 ± 4.789 cm. Considering that the total reaching length is 30 cm, it means that an average error of 32.38% occurs to the target point. Fig. 3.2(a) and (b) show the BMI system to provide a reference for the readers with regard to the degree of accuracy. Fig. 3.2(b) shows a miniaturized drawing of a real BMI system, although the palm of the adaptive robotic gripper is simplified as squares. The radius of the smaller transparent sphere around the target represents the TPE of the MEG. This implies that, on average, the center of the palm of the adaptive robotic gripper approached the surface of the transparent sphere.

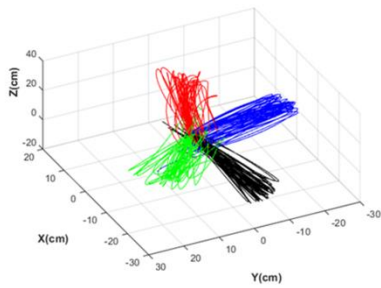
(a) Predicted Trajectory (MEG)



(c) Predicted Trajectory (EEG)



(b) Real Trajectory (MEG)



(d) Real Trajectory (EEG)

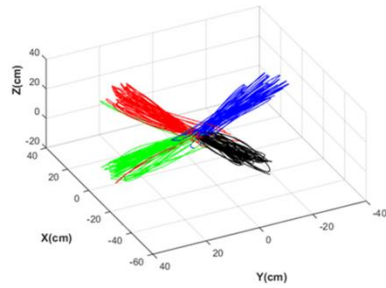


Fig. 3.1 Trajectories predicted from neural signals and real trajectories.

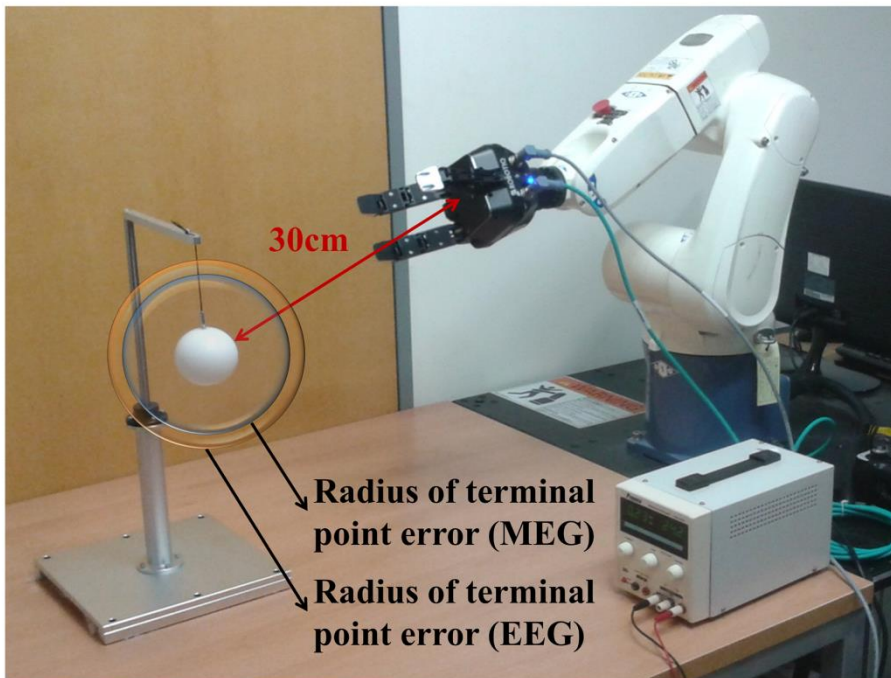
(a) Hand trajectories predicted by MEG (first session of subject 4). (b) Real hand trajectories reconstructed from the accelerometer signal during MEG signal acquisition (first session of subject 4). (c) Hand trajectories predicted by EEG (first session of subject 7). (d) Real hand trajectories reconstructed from the accelerometer signal during EEG signal acquisition (first session of subject 7). Each color represents one of the four hand-movement directions.

Table 3.1 Accuracy of the trajectories predicted with MEG

Subject	Session	Correlation	RMSE (cm)	TPE (cm)
1	1	0.726 (0.224)	10.041 (3.584)	11.040 (4.334)
	2	0.706 (0.216)	10.165 (3.458)	11.068 (4.490)
2	1	0.513 (0.381)	17.418 (7.194)	16.086 (6.086)
	2	0.569 (0.321)	16.953 (9.258)	4.027 (2.205)
3	1	0.812 (0.166)	13.383 (6.544)	6.499 (4.175)
	2	0.820 (0.188)	20.006 (70.367)	7.595 (4.786)
4	1	0.762 (0.219)	7.935 (3.147)	8.239 (3.241)
	2	0.800 (0.233)	6.919 (3.108)	6.787 (3.537)
5	1	0.754 (0.210)	8.560 (3.080)	8.086 (3.483)
	2	0.657 (0.269)	11.038 (4.098)	10.351 (4.849)
6	1	0.654 (0.265)	8.401 (3.299)	9.004 (4.372)
	2	0.770 (0.233)	6.811 (1.880)	8.391 (3.118)
7	1	0.728 (0.196)	10.304 (3.656)	10.564 (4.397)
	2	0.750 (0.210)	8.745 (3.098)	8.395 (4.076)
8	1	0.699 (0.274)	11.379 (6.137)	12.190 (5.771)
	2	0.762 (0.209)	10.522 (8.859)	11.621 (4.163)
9	1	0.620 (0.277)	11.022 (4.401)	11.346 (6.023)
	2	0.584 (0.246)	11.169 (3.924)	12.850 (6.033)
Average		0.705 (0.292)	11.154 (5.399)	9.714 (4.789)

Values in brackets represent standard deviations. * *Abbreviation*: root mean square error (RMSE), terminal point error (TPE).

(a)



(b)

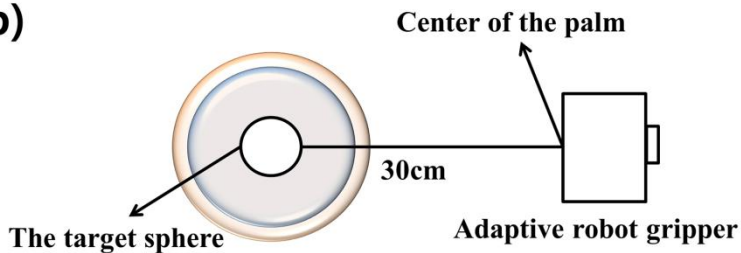


Fig. 3.2 TPE of MEG and EEG. (a) The distance between the target sphere and adaptive robotic gripper was 30 cm. The radius of the TPE is the average distance between the target sphere and adaptive robotic gripper at the closest position. (b) Miniaturized drawing of the real BMI system. Lengths are proportional to the actual size. * Abbreviation: terminal point error (TPE).

Then, 2,160 trials were conducted with EEG. As an example, Fig. 3.1(c) shows the predicted trajectories. Fig. 3.1(d) shows the real trajectories derived from the accelerometer. The same indexes were measured to evaluate the trajectory accuracy. These are listed in Table 3.2. The average correlation coefficients from each session were significant ($p < 0.011$ for the least accurate session). Further, the total correlation coefficient between the real and predicted trajectories was 0.684 ± 0.309 ($p < 0.001$) on average, and the RMSE was 13.724 ± 5.370 cm on average. The TPE was 11.432 ± 4.749 cm on average which indicates that an average error of 38.11% occurs to target point. The radius of the larger transparent sphere shown in Fig. 3.2 represents the TPE of the EEG.

Table 3.2 Accuracy of the trajectories predicted with EEG

Subject	Session	Correlation	RMSE (cm)	TPE (cm)
1	1	0.777 (0.204)	19.606 (58.826)	4.539 (2.771)
	2	0.745 (0.209)	11.569 (13.751)	11.915 (4.293)
2	1	0.743 (0.333)	14.908 (8.867)	12.007 (4.061)
	2	0.592 (0.255)	19.262 (37.090)	14.923 (4.700)
3	1	0.743 (0.202)	12.694 (17.501)	10.547 (4.033)
	2	0.756 (0.224)	11.065 (6.688)	9.923 (3.766)
4	1	0.587 (0.197)	15.007 (3.204)	13.643 (4.747)
	2	0.729 (0.205)	12.267 (2.833)	9.369 (3.005)
5	1	0.437 (0.459)	17.402 (10.729)	7.726 (5.526)
	2	0.439 (0.539)	17.590 (7.753)	8.854 (7.744)
6	1	0.635 (0.271)	14.435 (3.482)	8.486 (5.152)
	2	0.569 (0.308)	15.037 (3.454)	10.115 (4.403)
7	1	0.592 (0.277)	12.385 (3.259)	17.309 (4.899)
	2	0.820 (0.175)	11.011 (2.415)	13.828 (3.380)
8	1	0.787 (0.186)	12.225 (3.719)	14.689 (3.600)
	2	0.798 (0.129)	10.773 (3.181)	12.563 (3.875)
9	1	0.800 (0.155)	10.158 (2.485)	12.852 (4.224)
	2	0.765 (0.198)	9.638 (2.846)	12.482 (4.333)
Average		0.684 (0.309)	13.724 (5.370)	11.432 (4.749)

Values in brackets represent standard deviations. * *Abbreviation*: root mean square error (RMSE), terminal point error (TPE).

Comparison of MEG and EEG

The both trajectories predicted from MEG and EEG had a correlation coefficient of approximately 0.7. This implies that the predicted trajectories were significantly correlated to the real trajectories ($p < 0.03$ for all the sessions). According to the statistical analysis, EEG provided significantly less accuracy than MEG. Using an independent-sample comparison, we compared the three indexes. All three indexes with MEG were significantly ($p < 0.03$) better than those with EEG (see Tables 3.1 and 3.2). However, the practical values exhibited a small difference. The RMSE exhibited a difference of 2.566 cm, and the TPE exhibited a difference of only 1.717 cm. Fig. 3.2(b) shows that the two transparent spheres had a small size difference. The effect sizes listed in Table 3.3 (Cohen's $d < 0.50$) also demonstrate that the difference between EEG and MEG is not critical despite the proven statistical significance.

Table 3.3 Comparison of MEG and EEG

	Correlation	RMSE	TPE
<i>p</i> value	0.011	< 0.001	< 0.001
Cohen's <i>d</i>	0.070	0.477	0.360

In general, the effect size is not critical when Cohen's *d* is less than 0.5 [61].

Performance of Reaching and Grasping Motions

Before the reaching and grasping motions were performed, the accuracy of the IRAGS was verified in an environment using an approximately 2.3 kg robotic gripper fixed on the end-effector. Twelve trials (three trials per direction) were randomly selected among the predicted trajectories from the MEG and were used to verify the accuracy of the robot system. The RMSE between the input trajectory (predicted trajectory) and robot trajectory was $1.8 \times 10^{-3} \pm 3.3 \times 10^{-3}$ cm. It indicates an extremely small error, and no further calibration was required.

To verify the reaching and grasping motions, 80 trials from two sessions that demonstrated the median correlation coefficient were selected (40 trials from each session) as input data. The experiment was conducted with both EEG and MEG. Forty trials were randomly selected from the first session of subject 1 and the first session of subject 7 for MEG. For EEG, 40 trials were randomly selected from the first session of subject 2 and the first session of subject 3. The results were classified into three types: grasping, touching, and failure. These are shown in Fig. 3.3. A grasping success was counted as both grasping and touching. Out of the 80 trials, 15 trials (18.75%) with MEG and six trials (7.50%) with EEG succeeded at grasping, as listed in Table 3.4. However, the success rate was much higher for touching the target than grasping it. With MEG, 42 out of 80 trials (52.50%) succeeded in touching the

target. With EEG, 47 out of 80 trials (58.75%) succeeded in touching the target. The touching success rates were similar between MEG and EEG, whereas the grasping success rate was clearly higher in the MEG case.

Table 3.4 Success rates for grasping and touching

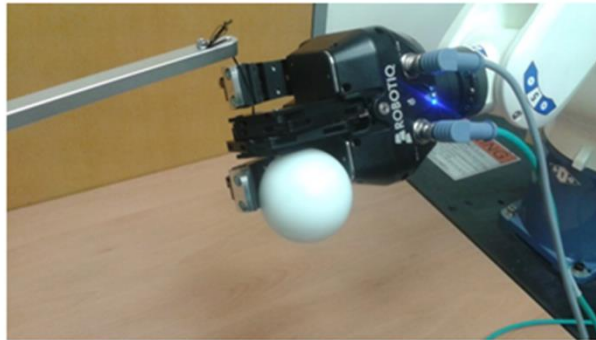
Signal Type	Grasping		Touching	
	No. of Successes	Success Rate	No. of Successes	Success Rate
MEG	15	18.75%	42	52.50%
EEG	6	7.50%	47	58.75%

MEG and EEG were each used in 80 trials.

(a)



(b)



(c)

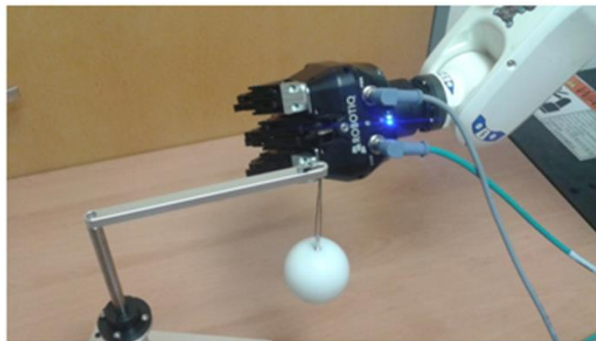


Fig. 3.3 Grasping and touching the target object. (a) Grasping. (b) Touching. (c) Failure.

3.2. Performance of Vision-Aided Training System

3.2.1. Target Object Detection and Position Estimation

No failure in target detection occurred. In all images, the correct number of targets were detected at the correct positions. Two target objects were photographed and the distance between the two targets was measured using both the calibrated Kinect and an optic tracker. The optic tracker was used as a gold standard because the commercial product had been validated as a highly accurate system. In the second approach, as represented in Table 3.5, the Kinect-based system exhibited a distance error of 0.0250 ± 0.0160 m compared with the optic tracker. This distance error is $4.620 \pm 3.490\%$ of the total distance between the two target objects, indicating that there is less than a 2-cm error when the robot conducts approximately 40 cm of reaching and grasping movements. When the size of the robotic gripper and the diameter of the target are considered, deviation of 1–2 cm is tolerable.

Table 3.5 Accuracy of the position estimation

No.	Distance measured using optic tracker (m)	Distance error (m)	Error percentage (%)
1	0.489	0.0158	3.221
2	0.589	0.0003	0.045
3	0.669	0.0197	2.949
4	0.430	0.0397	9.239
5	0.596	0.0401	6.725
6	0.572	0.0490	8.578
7	1.018	0.0238	2.335
8	1.013	0.0069	0.686
9	0.410	0.0373	9.106
10	0.519	0.0172	3.320
Average	0.630 ± 0.217	0.0250 ± 0.0160	4.620 ± 3.490

3.2.2. Trajectory Compensation

This study proposed a shared control algorithm using artificial potential and validated it using hand trajectories predicted from EEG signal. The algorithm was applied to 120 reaching trajectories in 4 directions. The target object positions were calculated using real hand trajectories, which were simultaneously measured with an accelerometer placed on the index finger. Applying this algorithm improved the predicted hand trajectories, and the shortest distance to the intended target object decreased, as shown in Fig. 3.4(a). Additionally, we can confirm that the three joint angles of the robotic arm continuously reached to the ideally required joint angle to reach the target (Fig. 3.4(b) and (c)). Fig. 3.5(a) shows the average improvement of the shortest distance to the target object as blending parameters differ. As blending parameters α and β increased, the degree of improvement increased. The shortest distance to the target decreased by 57.37% at both blending parameters were 1.00. It indicates that more than half of error to the target object at the closest point decreased. The patterns of improvement were similar for four each direction (Fig. 3.5(b)). Additionally, it was also confirmed that the algorithm with low blending parameter α worsen the performance of the BMI system. The decreased error lower than 0 in Fig. 3.5(b) indicates the shortest distance error to intended target object was increased.

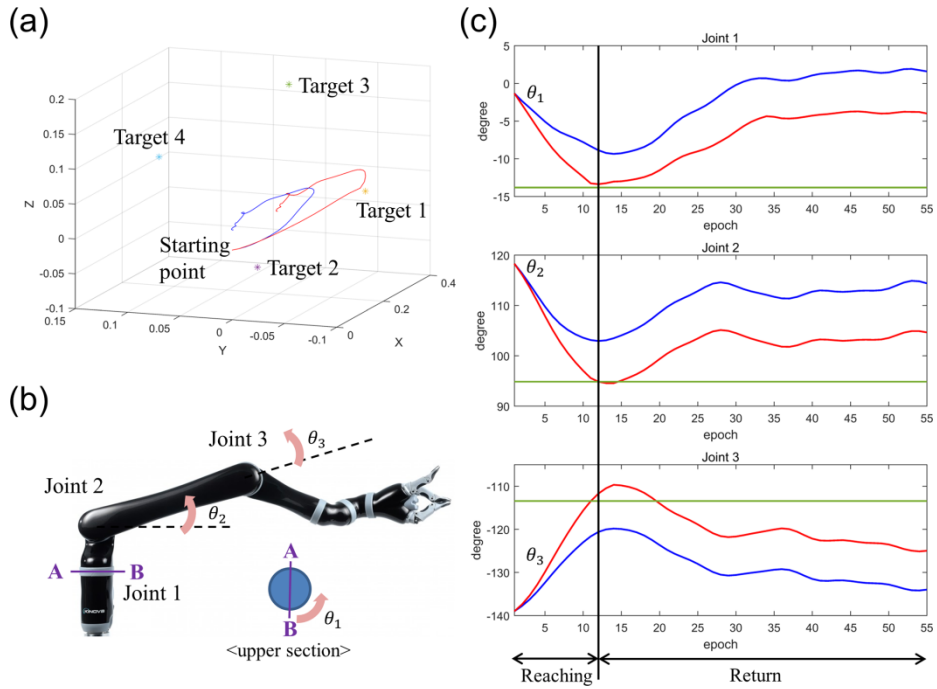


Fig. 3.4 (a) Compensated trajectory (red) reaches more closely to the target object than the raw hand trajectory predicted from EEG. (b) Definition of the joint angles of the robotic arm. (c) Green line indicates the ideal joint angle to reach the target object. Joint angles are closer to the ideal joint angles with compensation (red) than without (blue).

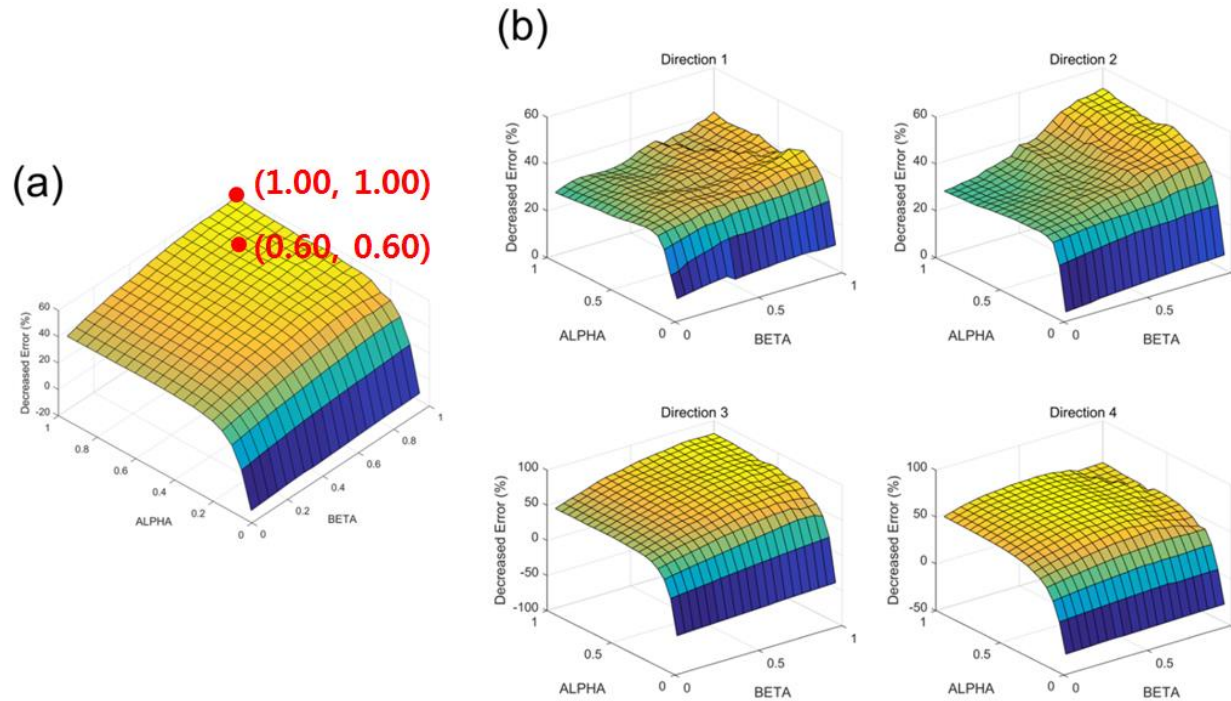


Fig. 3.5 (a) Decreased error to the intended target averaged over all 120 trials. Points with blending parameters $(\alpha, \beta) = (0.60, 0.60)$ and $(1.00, 1.00)$ are represented. (b) Decreased error to intended target averaged over 30 trials for individual directions.

Whereas the implemented algorithm using artificial potential enabled the robotic arm to more closely reach the intended target object, the shortest distance to non-intended target objects was not substantially affected by the algorithm. According to Fig. 3.6(a), the average shortest distance to the non-intended targets decreased by 4.07% at $\alpha = \beta = 1.00$. The degree of improvement was affected by α rather than β . The condition $\alpha = \beta = 0.60$ led to 5.84% improvement (Fig. 3.6(b)). In the individual cases of each of the four directions, less than 15% improvement was observed. The decrease in the shortest distance to the non-intended target was significantly less than that of the shortest distance to the intended target. Thus, it was confirmed that the algorithm enables the robot end-effector to selectively reach an intended target. The decrease in the shortest distances to the non-intended and intended targets were compared, as shown in Table 3.6. The p value, calculated using a one-tailed two-sample t-test, implies that the difference between the non-intended and intended targets was statistically significant. Fig. 3.7(a) and (b) show all the reaching trials before and after compensation, respectively ($\alpha = \beta = 0.60$; 1 of the 120 total trials is not represented, as it is a serious outlier).

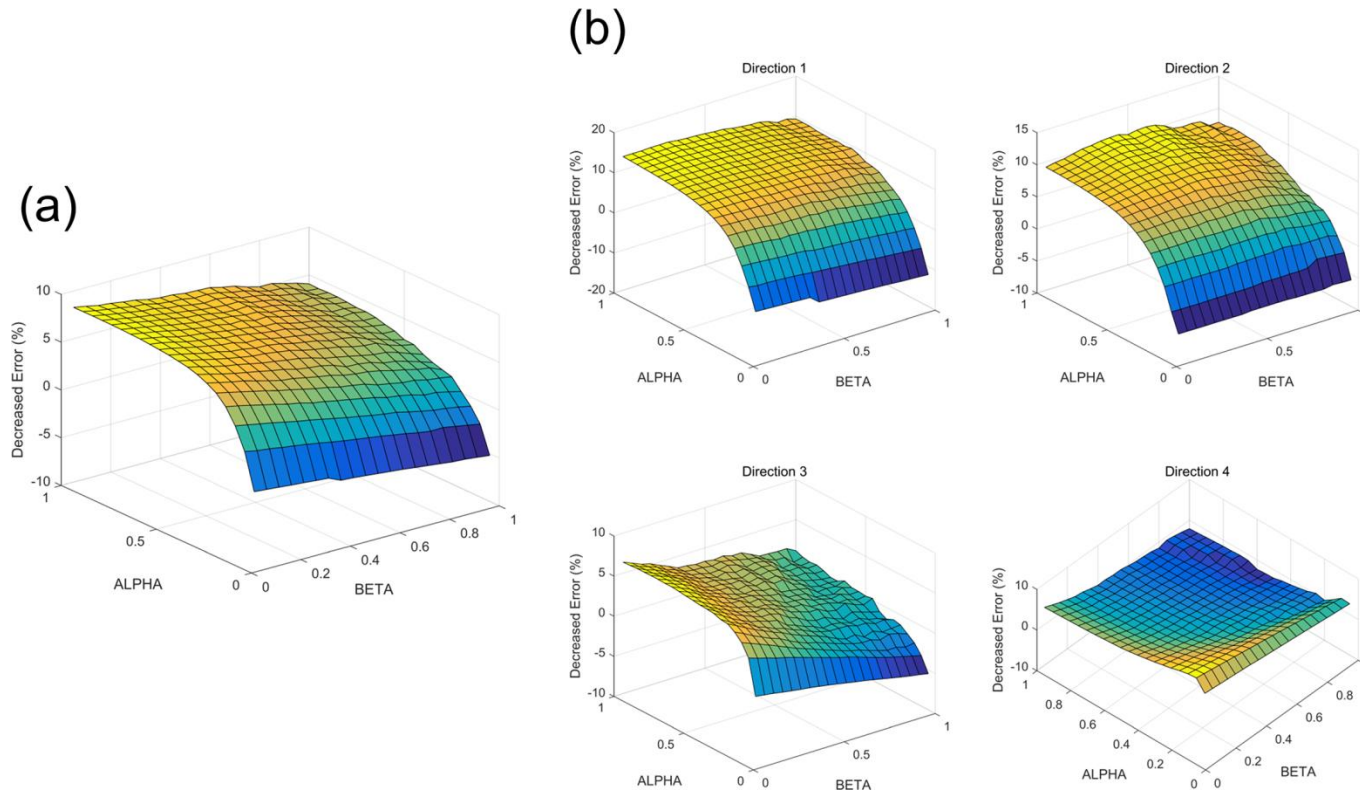


Fig. 3.6 (a) Decreased error to the three non-intended targets averaged over 120 trials. (b) Decreased error to the three non-intended targets averaged over 30 trials for each direction.

Table 3.6 Improvement of the predicted hand trajectory

$\alpha = \beta$	Decrease in the shortest distance to intended target (unit: %, n = 120)	Decrease in the shortest distance to non-intended target (unit: %, n = 360)	<i>p</i> value
1.00	57.37 ± 44.12	4.07 ± 29.18	< 0.0001
0.90	55.62 ± 43.63	4.70 ± 28.67	< 0.0001
0.80	54.73 ± 41.40	4.99 ± 26.22	< 0.0001
0.70	53.97 ± 37.16	5.58 ± 23.47	< 0.0001
0.60	51.85 ± 34.43	5.84 ± 20.40	< 0.0001
0.50	49.15 ± 32.60	5.89 ± 17.51	< 0.0001
0.40	46.63 ± 29.32	5.67 ± 14.74	< 0.0001
0.30	41.98 ± 27.12	5.26 ± 12.48	< 0.0001
0.20	33.02 ± 26.08	4.36 ± 12.27	< 0.0001
0.10	8.34 ± 36.43	1.19 ± 19.02	< 0.01

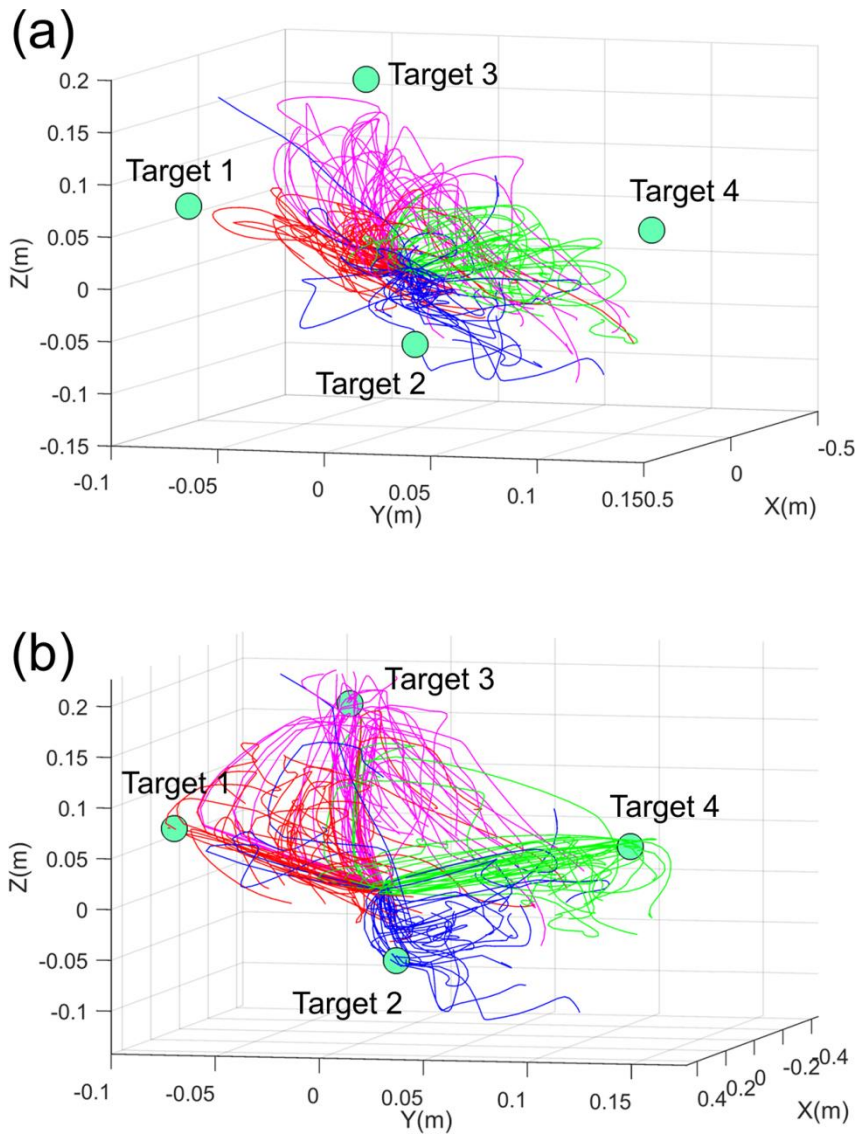


Fig. 3.7 (a) Raw hand trajectories predicted from EEG. (b) Compensated hand trajectories using artificial potential.

3.3. Effect of Training System in Two Clinical Cases

Before real-time BMI training with visual observation, both subjects showed brain activation in multiple areas in both hemispheres in fMRI findings. Subject #1 demonstrated significant brain activation in the precentral gyrus (primary motor cortex), postcentral gyrus (primary sensory cortex), posterior parietal cortex (PPC), and lateral portion of the middle frontal gyrus and inferior frontal gyrus (prefrontal cortex) in the right hemisphere, which correspond to the left hand the subject was trying to move (Fig. 3.8(a)). The contralateral cerebellum was also significantly activated (Fig. 3.8(a)). After real-time observation-based training, brain activation was focused to the right precentral and postcentral gyri, PPC, and contralateral cerebellum (Fig. 3.8(b)). Subject #2 also demonstrated scattered brain activation across both hemispheres (especially in the occipital lobe) before training; however, after training, the activated areas tended to focusing to the left precentral and postcentral gyri, PPC, and contralateral cerebellum, corresponding to the right hand the subject intended to move. However, in both cases, activation patterns did not differ between the three imagined reaching directions.

Although fMRI images showed meaningful focusing, shared control based on EEG decoding did not exceed the chance level (= 50%) significantly. Two subjects controlled robotic arm to reach instructed one out of two targets with

assist of shared control strategy. However, the success rate reaching the correct object did not show sufficient success rate because of low decoding power.

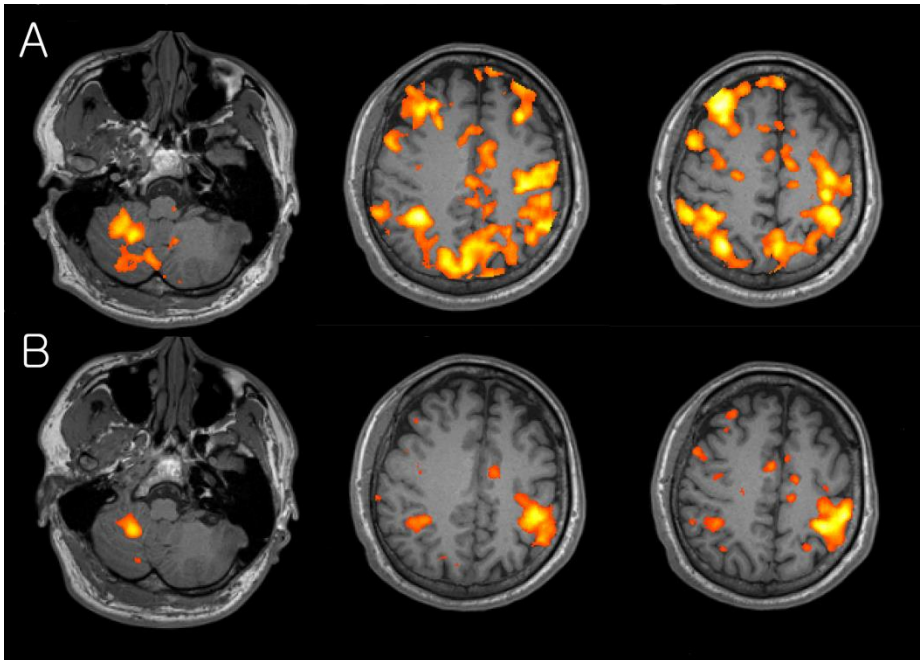


Fig. 3.8 (a) fMRI image during reaching task (left arm) in subject #1 shows brain activation in various area including right primary motor and sensory cortex, posterior parietal cortex, prefrontal cortex, and left cerebellum ($p < 0.001$). (b) Brain activation is relatively focused to the right primary motor and sensory cortex, posterior parietal cortex, and left cerebellum after 5 sessions of BMI training ($p < 0.001$).

4. Discussion

4.1. Evaluation for Hand Velocity Estimation

When the linear model of equation (2.1)-(2.3) was applied, both EEG and MEG exhibited a high correlation between the predicted and real trajectories. In particular, EEG showed an improved accuracy compared to the results of a previous EEG study [53]. In our study, three factors were mainly improved. First, the frequency band was changed to the broader pass band (0.5~8 Hz) to cover movement information of a higher frequency. Furthermore, sufficient rest time (4 s) was provided to exclude fluctuations from analysis. As a final factor, the study used data from a 200 ms interval (from -200 ms to present) whereas the previous EEG study used data from a 100 ms interval. The previous MEG study [54] showed that the correlation coefficient increases as the interval of preceding data increases. The three factors, which were already applied to the MEG study [54], contributed to the performance improvement not only for the MEG case but also for the EEG case.

Even though the trajectories were relatively accurate, they were not sufficient for performing reaching and grasping motions with a robotic arm gripper system, IRAGS. Three issues could be proposed as the reasons for the low

accuracy. The first is the limited spatial resolution of the non-invasive neural signals. Non-invasive neural signals are known to have a coarse spatial resolution, as shown in Fig. 1.1, because the electrodes are located on the surface of the human head and the area of a single electrode is relatively wide. In contrast, the invasive MEAs are implanted directly into the tissue of the human brain and make it possible to measure the spikes of single neuron.

The second factor is the inaccuracy of the accelerometer. In predicting movement using multiple linear regressions, acquisition of accurate weight matrices is crucial. The velocity information acquired from an accelerometer is used as reference data and is a critical factor for an accurate multiple linear regressions. However, the error accumulates during the integration process and an improved approach is required.

The third factor is the limitations of linear regression. Linear models give limited predictability in reconstructing hand trajectory. More complex methods such as nonlinear approaches can demonstrate a more improved result. However, with respect to on-line control rather than reconstruction, linear models such as PVA and OLE have been used because simple models are more intuitive for user to adapt [48]. Thus, complicated nonlinear models are not appropriate, even though they provide a more powerful reconstruction performance.

The success rate for grasping turned out to need some improvements from a practical point-of-view. Even though the success rate for grasping was not

sufficiently high, the robot was able to approach the target very closely. In most of the trials, and more than half of the trials resulted in touching. Hochberg's study showed that the MEA-based on-line control succeeded in contacting the target object with an accuracy of $65.94 \pm 19.88\%$ on average [2]. The touching accuracy represented in table 3.4 is close to the results of the invasive study. Even though the comparison of our reconstruction study with the on-line control study is not completely appropriate, it has a satisfactory success rate. The use of additional sensors may be a powerful method of improving the success rate. Onose et al. [36] used a pair of cameras to find the 3D gaze point and succeeded in reaching and grasping objects with EEG. Kim et al. [43] controlled a robotic arm with the assistance of external sensors and greatly improved the performance of the reaching and grasping motions. They were the first to apply continuous shared control (CSC) which was initially proposed to help humans intervene in autonomous tasks executed by a robot [62] to a BMI. Kennel et al. used a stereo camera with a robotic arm controlled by MEG to grasp a target object [63]. Some studies have implemented BMI systems based on non-invasive neural signals assisted by external sensors in systems other than robotic arms [64, 65]. Yeom et al. proposed using an image processing technique [66] and Kalman filtering [67] to improve the accuracy of the predicted hand trajectories.

Although MEG has better spatial resolution than EEG, an MEG device is not portable and requires a magnetically shielded room. Therefore, EEG should be used for real-time operation. The results of this study showed that EEG

provided a comparable performance to that of MEG. Even though the trajectory predicted with EEG was statistically not as accurate as that with MEG, the practical difference was small. In particular, the TPE, which is crucial index for reaching and grasping, exhibited a difference of only 1.717cm (5.72% of total reaching distance). The effect size also demonstrated that the difference between MEG and EEG is not critical (Cohen's $d < 0.50$). In addition, the success rate for touching (see Table 3.4) supported the competitiveness of EEG. As mentioned in the Materials and Methods section, EEG channels were distributed over the entire head, whereas MEG channels were distributed at the motor-related area. In addition, 64 channels were used for EEG, whereas 68 channels were used for MEG. Based on these factors, the EEG accuracy could be improved by locating more channels in the motor-related area. Use of a 128-channel EEG system could be an alternative. Therefore, an EEG-driven robot, which is a portable system, can potentially be realized.

Another issue was that orientation was not considered in the decoding model. In the off-line robotic arm control used for validation, the three-DOF for orientation were fixed as constant values. Although recent invasive studies [23, 48] used seven-DOF model for robotic arm control, research on three-DOF translation motion should be preceded to reach next step for three-DOF of orientation and one-DOF grasping motion. The orientation and grasping motion are expected to be controlled automatically depending on the external sensor and intelligent algorithm rather than neural signal.

4.2. Evaluation for Vision-Aided Training System

The vision-aided system consists of an anthropomorphic robotic arm, Kinect, and targets. The Kinect enables target object detection and position estimation. In 60 validation trials (20 each for 2, 3, and 4 target objects), there were no failures in target detection. The implemented target detection algorithm can automatically detect multiple targets; however, it is still limited in that target objects must be specified with specific colors and the performance can deteriorate for an increased number of target objects. To extend the use of the developed system to ADL, an improved algorithm with shape-based target detection is required. Improved image processing approaches, such as a convolutional neural network (CNN) [68, 69], or a histogram of oriented gradients [70, 71], could potentially be applied as appropriate alternatives to overcome this issue.

The position estimation error rate was about 4.62%, and occurred for two main reasons. First, the calibration approach is linear. For camera calibration and position estimation, we applied linear regression using the least-squares method. Even though this approach performed satisfactorily, it cannot fully explain the complicated relations between variables, and thus yields error. Second, the implemented algorithm estimated the center of two target objects, whereas the optic tracker measured the distance between stickers, causing differences between the two results.

A shared control strategy was used to compensate for the joint movement of the robotic arm and reach closer to the intended target. We found that the motion planning approach improved the shortest distance to the intended target up to 57.37%, whereas that of the non-intended targets showed almost no improvement. The t-test results supported this observation statistically ($p < 0.0001$). This results implies that the target, which the robot reached with the shared control strategy, no longer needs to be preprogrammed as in previous studies [23, 48]. A user of the developed training system can arbitrarily select a target object from several objects without any preprogrammed information. Since the intended object is updated every moment, it is also possible to modify the target object in the middle of the trial. Although shared control based on high-level commands (a goal-oriented approach) frees the system from the burden of low-level and demanding high-speed interaction, it limits the robotic arm to preprogrammed commands [72]. The suggested process-oriented approach provides a low-level intervention in the robotic arm movement and does not highly limit the paths by which the robot moves. Thus, the suggested algorithm preserves the high level of user volition for the robotic arm control. These characteristics give the training system the following advantages. First, it is easy to set the appropriate chance level for active shared control. Since active shared control can reach a target even with random walk signal through an auxiliary control command, reaching the target point is not a measure of success. Rather, it is a more objective indicator of success to reach the intended target among various candidate objects. In this case, the chance level is calculated as in equation 1.9. Second, it is easy to

perform robust parameter training because the targets can be moved by using flexible cable as used in the current study. Trained model parameters for targets at various locations can avoid the issue of the decoding model being over-fitted to objects at specific locations. In addition, the reaching success rate of the target object at any arbitrary position can give a higher sense of trust to the reader of a paper or the viewer of a video. Third, its use can be extended to the purpose of ADL. If an artificial intelligence that detects several objects used in daily living is added, it is expected to be more useful than existing algorithms in that the robot can reach to an intended target among several candidate objects. Thus, the proposed approach is highly practical for both training and ADL, compared to those proposed previously.

At blending parameters $\alpha = \beta = 0.60$, the degree of improvement is sufficiently saturated, such that the shortest distance to the intended target decreased by 51.85%, which is approximately 90% of 57.37%. According to Table 4.1, the degree of improvement is sufficiently saturated at the condition $\alpha = \beta = 0.60$. In the case of Direction 4, the condition in which $\alpha = \beta = 0.60$ (60.49%) exhibited a greater improvement than the condition in which $\alpha = \beta = 1.00$ (55.28%); therefore, it is inferred that blending parameters exceeding 0.60 are not highly effective. Considering that users prefer the BMI training system with lower blending parameters, which indicates high volition and inertia, $\alpha = \beta = 0.60$ is the optimal condition.

Table 4.1 Improvement of the predicted hand trajectory at $\alpha = \beta = 0.60$ and 1.00

(α, β)	Direction 1 (%)	Direction 2 (%)	Direction 3 (%)	Direction 4 (%)	Average (%)
(1.00, 1.00)	41.12	51.20	81.90	55.28	57.37
(0.60, 0.60)	36.20	37.18	73.55	60.49	51.85

In the first phase of training (first 5 training sessions), the subjects were given a VR video of robotic motion for motor imagery of reaching motion, as the purpose of this phase was to accustom them to the imagery task. Users were instructed to assume that the robotic arm was their arm, as the robotic arm was positioned nearest to their paralyzed arm. However, even after 5 sessions of imagery training, fMRI revealed that brain activation areas were scattered across motor planning and execution areas in both hemispheres. This result suggested a less characterized pattern of brain activity, although the most significantly active areas were consistent with previous studies reporting areas activated during motor imagery and BMI learning: the ipsilateral premotor cortex, supplementary motor area, primary motor cortex, PPC, insula, and contralateral cerebellum [73, 74].

After 5 additional training sessions with the observation-based training provided, brain activation patterns tended to focus on the primary motor and sensory areas, PPC, and contralateral cerebellum. Wander et al. [75] also demonstrated that cortical adaptation occurs during BMI learning, during which activation in the prefrontal cortex, premotor cortex, and PPC tend to decrease as users switch from cognitive to automatic phases. However, in our study, while prefrontal and premotor cortex activity decreased significantly, PPC activity was relatively sustained. This difference may arise from the fact that the subjects were still in the training phase of the external robot control, which may require PPC and cerebellar activity for planning movements and BMI learning [76], even if imagining the reaching movement itself may have

entered the autonomic phase, requiring less prefrontal and premotor activity. This result suggests that the reorganization and plasticity of the brain play an essential role in BMI training, in addition to the algorithm-based training of the system, such as machine learning methods. Cortical reorganization during the BMI training for reaching and grasping or neurofeedback in rehabilitation has also been shown in other studies [77, 78]. Because the gross activation pattern significantly changes with repeated training, the decoding parameters should be updated with each training session.

By comparing the first 5 sessions of the VR-based training and the last 5 sessions of the observation-based training, the focus of the brain activation had obviously proceeded further than in the first phase. It indicates that observing the actual robot is more effective for BMI training than looking at the VR video. However, further research is required to generalize this opinion as only two subjects participated in the experiment.

Using the proposed shared control strategy for the robot end-effector to reach the intended target, the success rate of reaching the instructed target did not exceed the chance level significantly. It is possible that, as we could not confirm the difference in brain activation according to the direction of motion imagery in fMRI, it may be necessary to observe the activation with electrodes of a higher spatial resolution in the area where activation is focused. At least, it is almost certain that EEG cannot distinguish the pattern inside the active area of the fMRI image in Fig. 3.8(b).

5. Conclusion

BMIs allow a person to bypass the conventional neuromuscular pathways to interact with the environment via an analysis of the electrical brain activation. Whereas recent invasive studies reported seven-DOF robotic arm control based on motor imagery, non-invasive studies have not reached that stage yet. Although there are inherent limitations owing to the spatial resolution of EEG, the advantage of non-invasiveness provides sufficient need for ongoing research. Thus, in this study, three additional steps were attempted in addition to the previous studies.

In the first step, a linear model for three DOF of translational motion was tried. The linear model exhibited sufficient decoding performance for hand trajectory reconstruction compared to a previous EEG based study [53]. The reconstructed trajectory could reach a position with 38.11% distance error to the target surface on average when reaching motions of 30 cm length were performed.

In the second step, this study suggested and developed a BMI training system based on an active shared control strategy. When compared to previous training systems, it is possible to detect and estimate the position of multiple targets, and the shared control strategy enables the robot end-effector to reach the intended targets out of a range of detected ones. It does not require a

preprogrammed target and allows the user to reflect more volition. Furthermore, with slight improvements, the application range can be extended to be used for ADL.

In the third step, the developed training system was applied to two potential users with cervical SCI. The pilot clinical study, utilizing the observation-based training, suggested potential beneficial effects in characterizing the brain activation patterns. Using the proposed shared control for the robot end-effector to reach the intended target, the success rate of reaching the instructed target did not exceed the chance level significantly, and the limited spatial resolution of EEG could be a possible reason when the size of the activation area of fMRI is considered.

Through this study, a linear decoding model for hand velocity estimation was verified, and a vision-aided BMI training system was developed. Based on observation-based training using the developed system, subjects with cervical SCI showed brain activation patterns with a tendency toward meaningful focusing.

References

- [1] M. Atzori and H. Muller, "Control Capabilities of Myoelectric Robotic Prostheses by Hand Amputees: A Scientific Research and Market Overview," *Front Syst Neurosci*, vol. 9, no. 162, 2015.
- [2] L. R. Hochberg, D. Bacher, B. Jarosiewicz, N. Y. Masse, J. D. Simeral, J. Vogel, et al., "Reach and grasp by people with tetraplegia using a neurally controlled robotic arm," *Nature*, vol. 485, no. 7398, pp. 372-5, 2012.
- [3] G. Buzsáki, C. Anastassiou, and C. Koch, "The origin of extracellular fields and currents—EEG, ECoG, LFP and spikes," *Nat Rev Neurosci*, vol. 13, no. 6, pp. 407-20, 2012.
- [4] M. Alam, W. Rodrigues, B. N. Pham, and N. V. Thakor, "Brain-machine interface facilitated neurorehabilitation via spinal stimulation after spinal cord injury: Recent progress and future perspectives," *Brain Res*, vol. 1646, pp. 25-33, 2016.
- [5] J. N. Mak and J. R. Wolpaw, "Clinical Applications of Brain-Computer Interfaces: Current State and Future Prospects," *IEEE Rev Biomed Eng*, vol. 2, pp. 187-99, 2009.
- [6] N. Thakor. (2012). Building brain machine interfaces—neuroprosthetic control with electrocorticographic signals

[<http://lifesciences.ieee.org/publications/newsletter/april-2012/96-building-brain-machine-interfaces-neuroprosthetic-control-with-electrocorticographic-signals>].

- [7] A. Gilletti and J. Muthuswamy, "Brain micromotion around implants in the rodent somatosensory cortex," *J Neural Eng*, vol. 3, pp. 189-95, 2006.
- [8] S. F. Cogan, "Neural stimulation and recording electrodes," *Annu Rev Biomed Eng*, vol. 10, pp. 275-309, 2008.
- [9] V. S. Polikov, P. A. Tresco, and W. M. Reichert, "Response of brain tissue to chronically implanted neural electrodes," *J Neurosci Methods*, vol. 148, pp. 1-18, 2005.
- [10] B. A. Kakulas, "A review of the neuropathology of human spinal cord injury with emphasis on special features," *J Spinal Cord Med*, vol. 22, pp. 119-24, 1999.
- [11] S. Harkema, Y. Gerasimenko, J. Hodes, J. Burdick, C. Angeli, Y. Chen, et al., "Effect of epidural stimulation of the lumbosacral spinal cord on voluntary movement, standing, and assisted stepping after motor complete paraplegia: a case study," *Lancet*, vol. 377, pp. 1938-47, 2011.
- [12] V. R. Edgerton and R. R. Roy, "A new age for rehabilitation," *Eur J Phys Rehabil Med*, vol. 48, pp. 99-109, 2012.
- [13] J. V. Lynskey, A. Belanger, and R. Jung, "Activity-dependent

- plasticity in spinal cord injury," *J Rehabil Res Dev*, vol. 45, pp. 229-40, 2008.
- [14] R. R. Roy, S. J. Harkema, and V. R. Edgerton, "Basic concepts of activity-based interventions for improved recovery of motor function after spinal cord injury," *Arch Phys Med Rehabil*, vol. 93, pp. 1487-97, 2012.
- [15] A. Jackson and J. B. Zimmermann, "Neural interfaces for the brain and spinal cord--restoring motor function," *Nat Rev Neurol*, vol. 8, pp. 690-9, 2012.
- [16] A. L. Orsborn, H. G. Moorman, S. A. Overduin, M. M. Shanechi, D. F. Dimitrov, and J. M. Carmena, "Closed-loop decoder adaptation shapes neural plasticity for skillful neuroprosthetic control," *Neuron*, vol. 82, pp. 1380-93, 2014.
- [17] E. E. Fetz, "Restoring motor function with bidirectional neural interfaces," *Prog Brain Res*, vol. 218, pp. 241-52, 2015.
- [18] J. R. Wolpaw, N. Birbaumer, D. J. McFarland, G. Pfurtscheller, and T. M. Vaughan, "Brain-computer interfaces for communication and control," *Clin Neurophysiol*, vol. 113, pp. 767-91, 2002.
- [19] J. P. Donoghue, "Connecting cortex to machines: recent advances in brain interfaces," *Nat Neurosci*, vol. 5, pp. 1085-8, 2002.

- [20] A. B. Schwartz, "Cortical neural prosthetics," *Annu Rev Neurosci*, vol. 27, pp. 487-507, 2004.
- [21] M. A. Lebedev and M. A. Nicolelis, "Brain-machine interfaces: past, present and future," *Trends Neurosci*, vol. 29, pp. 536-46, 2006.
- [22] M. Velliste, S. Perel, M. C. Spalding, A. S. Whitford, and A. B. Schwartz, "Cortical control of a prosthetic arm for self-feeding," *Nature*, vol. 453, pp. 1098-101, 2008.
- [23] J. L. Collinger, B. Wodlinger, J. E. Downey, W. Wang, E. C. Tyler-Kabara, D. J. Weber, et al., "High-performance neuroprosthetic control by an individual with tetraplegia," *Lancet*, vol. 381, pp. 557-64, 2013.
- [24] S.-J. Kim, S. C. Manyam, D. J. Warren, and R. A. Normann, "Electrophysiological mapping of cat primary auditory cortex with multielectrode arrays," *Ann Biomed Eng*, vol. 34, pp. 300-9, 2006.
- [25] I. Pathirage, K. Khokar, E. Klay, R. Alqasemi, and R. Dubey, "A vision based P300 brain computer interface for grasping using a wheelchair-mounted robotic arm," in *Advanced Intelligent Mechatronics (AIM), 2013 IEEE/ASME International Conference on*, 2013, pp. 188-93.
- [26] S. Mohammed, J. C. Moreno, K. Kong, and Y. Amirat,

Intelligent assistive robots: recent advances in assistive robotics for everyday activities, vol. 106, Springer, 2015.

- [27] M. Palankar, K. J. De Laurentis, R. Alqasemi, E. Veras, R. Dubey, Y. Arbel, et al., "Control of a 9-DoF wheelchair-mounted robotic arm system using a P300 brain computer interface: Initial experiments," in *Robotics and Biomimetics, 2008. ROBIO 2008. IEEE International Conference on*, 2009, pp. 348-53.
- [28] J. S. Blasco, E. Iáñez, A. Úbeda, and J. M. Azorín, "Visual evoked potential-based brain-machine interface applications to assist disabled people," *Expert Syst Appl*, vol. 39, pp. 7908-18, 2012.
- [29] D. Valbuena, M. Cyriacks, O. Friman, I. Volosyak, and A. Graser, "Brain-Computer Interface for high-level control of rehabilitation robotic systems," in *2007 IEEE 10th International Conference on Rehabilitation Robotics*, 2007, pp. 619-25.
- [30] H. Bakardjian, T. Tanaka, and A. Cichocki, "Brain control of robotic arm using affective steady-state visual evoked potentials," in *Proceedings of the 5th IASTED International Conference Human-Computer Interaction*, 2010, pp. 264-70.
- [31] R. Ortner, B. Z. Allison, G. Korisek, H. Gaggl, and G. Pfurtscheller, "An SSVEP BCI to control a hand orthosis for

- persons with tetraplegia," *IEEE Trans Neural Syst Rehabil Eng*, vol. 19, pp. 1-5, 2011.
- [32] T. Sakurada, T. Kawase, K. Takano, T. Komatsu, and K. Kansaku, "A BMI-based occupational therapy assist suit: asynchronous control by SSVEP," *Front Neurosci*, vol. 7, p. 172, 2013.
- [33] E. Hortal, D. Planelles, A. Costa, E. Iáñez, A. Úbeda, J. M. Azorín, et al., "SVM-based Brain–Machine Interface for controlling a robot arm through four mental tasks," *Neurocomputing*, vol. 151, pp. 116-121, 2015.
- [34] A. Úbeda, E. Iáñez, J. Badesa, R. Morales, J. M. Azorín, and N. García, "Control strategies of an assistive robot using a Brain-Machine Interface," in *Intelligent Robots and Systems (IROS), 2012 IEEE/RSJ International Conference on*, 2012, pp. 3553-8.
- [35] J. Meng, S. Zhang, A. Bekyo, J. Olsoe, B. Baxter, and B. He, "Noninvasive electroencephalogram based control of a robotic arm for reach and grasp tasks," *Sci Rep*, vol. 6, 38565, 2016.
- [36] G. Onose, C. Grozea, A. Anghelescu, C. Daia, C. Sinescu, A. Ciurea, et al., "On the feasibility of using motor imagery EEG-based brain–computer interface in chronic tetraplegics for assistive robotic arm control: a clinical test and long-term post-trial follow-up," *Spinal Cord*, vol. 50, pp. 599-608, 2012.

- [37] S. Bhattacharyya, A. Konar, and D. N. Tibarewala, "Motor imagery, P300 and error-related EEG-based robot arm movement control for rehabilitation purpose," *Med Biol Eng Comput*, vol. 52, pp. 1007-17, 2014.
- [38] E. Muglerab, M. Benschc, S. Haldera, W. Rosenstielc, M. Bogdand, N. Birbaumerae, et al., "Control of an internet browser using the P300 event-related potential," *Int J Bioelectromagn*, vol. 10, pp. 56-63, 2008.
- [39] G. D. Johnson and D. J. Krusienski, "Ensemble SWLDA classifiers for the P300 speller," in *International Conference on Human-Computer Interaction*, 2009, pp. 551-7.
- [40] L. A. Farwell and E. Donchin, "Talking off the top of your head: toward a mental prosthesis utilizing event-related brain potentials," *Electroencephalogr Clin Neurophysiol*, vol. 70, pp. 510-23, 1988.
- [41] F. Beverina, G. Palmas, S. Silvoni, F. Piccione, and S. Giove, "User adaptive BCIs: SSVEP and P300 based interfaces," *PsychNology Journal*, vol. 1, pp. 331-54, 2003.
- [42] J. Decety and M. Lindgren, "Sensation of effort and duration of mentally executed actions," *Scandinavian journal of psychology*, vol. 32, pp. 97-104, 1991.
- [43] H. K. Kim, S. J. Biggs, D. W. Schloerb, J. M. Carmena, M. A.

- Lebedev, M. A. Nicolelis, et al., "Continuous shared control for stabilizing reaching and grasping with brain-machine interfaces," *IEEE Trans Biomed Eng*, vol. 53, pp. 1164-73, 2006.
- [44] J. E. Downey, J. M. Weiss, K. Muelling, A. Venkatraman, J.-S. Valois, M. Hebert, et al., "Blending of brain-machine interface and vision-guided autonomous robotics improves neuroprosthetic arm performance during grasping," *J Neuroeng Rehabil*, vol. 13, no. 28, 2016.
- [45] D. P. McMullen, G. Hotson, K. D. Katyal, B. A. Wester, M. S. Fifer, T. G. McGee, et al., "Demonstration of a semi-autonomous hybrid brain-machine interface using human intracranial EEG, eye tracking, and computer vision to control a robotic upper limb prosthetic," *IEEE Trans Neural Syst Rehabil Eng*, vol. 22, pp. 784-96, 2014.
- [46] K. D. Katyal, M. S. Johannes, S. Kellis, T. Aflalo, C. Klaes, T. G. McGee, et al., "A collaborative BCI approach to autonomous control of a prosthetic limb system," in *2014 IEEE International Conference on Systems, Man, and Cybernetics (SMC)*, 2014, pp. 1479-82.
- [47] A. Georgopoulos, J. Kalaska, R. Caminiti, and J. Massey, "On the relations between the direction of two-dimensional arm movements and cell discharge in primate motor cortex," *J*

- Neurosci, vol. 2, pp. 1527-37, 1982.
- [48] S. T. Clanton, Brain-computer interface control of an anthropomorphic robotic arm, Ph.D. Thesis, Carnegie Mellon University, 2011.
- [49] W. Wang, S. S. Chan, D. A. Heldman, and D. W. Moran, "Motor cortical representation of position and velocity during reaching," *J Neurophysiol*, vol. 97, pp. 4258-70, 2007.
- [50] Virtual Fixture [https://en.wikipedia.org/wiki/Virtual_fixture].
- [51] Y. J. Kim, S. W. Park, H. G. Yeom, M. S. Bang, J. S. Kim, C. K. Chung, et al., "A study on a robot arm driven by three-dimensional trajectories predicted from non-invasive neural signals," *Biomed Eng Online*, vol. 14, no. 81, 2015.
- [52] T. Mulder, "Motor imagery and action observation: cognitive tools for rehabilitation," *J Neural Transm*, vol. 114, pp. 1265-78, 2007.
- [53] T. J. Bradberry, R. J. Gentili, and J. L. Contreras-Vidal, "Reconstructing three-dimensional hand movements from noninvasive electroencephalographic signals," *J Neurosci*, vol. 30, pp. 3432-7, 2010.
- [54] H. G. Yeom, J. S. Kim, and C. K. Chung, "Estimation of the velocity and trajectory of three-dimensional reaching movements from non-invasive magnetoencephalography

- signals," *J Neural Eng*, vol. 10, no. 2, 2013.
- [55] J. Rickert, S. C. de Oliveira, E. Vaadia, A. Aertsen, S. Rotter, and C. Mehring, "Encoding of Movement Direction in Different Frequency Ranges of Motor Cortical Local Field Potentials," *J Neurosci*, vol. 25, pp. 8815-24, 2005.
- [56] S. Waldert, H. Preissl, E. Demandt, C. Braun, N. Birbaumer, A. Aertsen, et al., "Hand movement direction decoded from MEG and EEG," *J Neurosci*, vol. 28, pp. 1000-8, 2008.
- [57] G. Pfurtscheller and F. H. Lopes da Silva, "Event-related EEG/MEG synchronization and desynchronization: basic principles," *Clin Neurophysiol*, vol. 110, pp. 1842-57, 1999.
- [58] N. Bennis and A. Roby-Brami, "Coupling between reaching movement direction and hand orientation for grasping," *Brain Res*, vol. 952, pp. 257-67, 2002.
- [59] L. S. Bruno Siciliano, Luigi Villani, and Giuseppe Oriolo, *Robotics Modelling, Planning and Control*, Springer, 2009.
- [60] A. Lopes, J. Rodrigues, J. Perdigao, G. Pires, and U. Nunes, "A New Hybrid Motion Planner: Applied in a Brain-Actuated Robotic Wheelchair," *IEEE Robot Autom Mag*, vol. 23, no. 4, pp. 82-93, 2016.
- [61] J. Cohen, *Statistical power ANALYSIS for the Behavioral sciences*, 2nd ed., Lawrence Erlbaum Associates, 1988.

- [62] K. Salisbury, "Issues in human/computer control of dexterous remote hands," *IEEE Trans Aerosp Electron Syst*, vol. 24, pp. 591-6, 1988.
- [63] M. Kennel, H. Hinrichs, C. Reichert, J. W. Rieger, and U. Schmucker, "A robot for brain-controlled grasping," presented at the HRI 2014 Workshop, 2014.
- [64] Jd. R. Millan, F. Renkens, J. Mourino, and W. Gerstner, "Noninvasive brain-actuated control of a mobile robot by human EEG," *IEEE Trans Biomed Eng*, vol. 51, pp. 1026-33, 2004.
- [65] T. Carlson and Jd. R. Millan, "Brain-Controlled Wheelchairs: A Robotic Architecture," *IEEE Robot Autom Mag*, vol. 20, pp. 65-73, 2013.
- [66] H. G. Yeom, J. S. Kim, and C. K. Chung, "High-Accuracy Brain-Machine Interfaces Using Feedback Information," *PLoS ONE*, vol. 9, e103539, 2014.
- [67] H. G. Yeom, W. Hong, D.-Y. Kang, C. K. Chung, J. S. Kim, and S.-P. Kim, "A Study on Decoding Models for the Reconstruction of Hand Trajectories from the Human Magnetoencephalography," *Biomed Res Int*, vol. 2014, 176857, 2014.
- [68] Y. LeCun, Y. Bengio, and G. Hinton, "Deep Learning," *Nature*

vol. 521, no. 7553, pp. 436-44, 2015.

- [69] A. Krizhevsky, I. Sutskever, and G. E. Hinton, "ImageNet classification with deep convolutional neural networks," presented at the Proceedings of the 25th International Conference on Neural Information Processing Systems - Volume 1, Lake Tahoe, Nevada, 2012.
- [70] N. Dalal and B. Triggs, "Histograms of oriented gradients for human detection," in 2005 IEEE Computer Society Conference on Computer Vision and Pattern Recognition (CVPR'05), 2005, pp. 886-93.
- [71] Z. Qiang, Y. Mei-Chen, C. Kwang-Ting, and S. Avidan, "Fast Human Detection Using a Cascade of Histograms of Oriented Gradients," in 2006 IEEE Computer Society Conference on Computer Vision and Pattern Recognition (CVPR'06), 2006, pp. 1491-8.
- [72] B. Z. Allison, R. Leeb, C. Brunner, G. R. Muller-Putz, G. Bauernfeind, J. W. Kelly, et al., "Toward smarter BCIs: extending BCIs through hybridization and intelligent control," *J Neural Eng*, vol. 9, 013001, 2012.
- [73] S. Marchesotti, R. Martuzzi, A. Schurger, M. L. Blefari, J. R. Del Millan, H. Bleuler, et al., "Cortical and subcortical mechanisms of brain-machine interfaces," *Hum Brain Mapp*,

vol. 38, pp. 2971-89, 2017.

- [74] S. V. Hiremath, W. Chen, W. Wang, S. Foldes, Y. Yang, E. C. Tyler-Kabara, et al., "Brain computer interface learning for systems based on electrocorticography and intracortical microelectrode arrays," *Front Integr Neurosci*, vol. 9, no. 40, 2015.
- [75] J. D. Wander, T. Blakely, K. J. Miller, K. E. Weaver, L. A. Johnson, J. D. Olson, et al., "Distributed cortical adaptation during learning of a brain-computer interface task," *Proc Natl Acad Sci U S A*, vol. 110, pp. 10818-23, 2013.
- [76] D. Baldauf, H. Cui, and R. A. Andersen, "The posterior parietal cortex encodes in parallel both goals for double-reach sequences," *J Neurosci*, vol. 28, no. 40, pp. 10081-9, 2008.
- [77] J. Ushiba and S. R. Soekadar, "Brain-machine interfaces for rehabilitation of poststroke hemiplegia," *Prog Brain Res*, vol. 228, pp. 163-83, 2016.
- [78] J. M. Carmena, M. A. Lebedev, R. E. Crist, J. E. O'Doherty, D. M. Santucci, D. F. Dimitrov, et al., "Learning to control a brain-machine interface for reaching and grasping by primates," *PLoS Biol*, vol. 1, E42, 2003.

Abstract in Korean

국문초록

사람들은 뇌졸중, 루게릭병, 그리고 척수 손상과 같은 다양한 질병 및 물리적인 사고로 운동 기능의 일부 혹은 전부를 상실할 수 있으며, 이로 인해 일상생활에 많은 어려움을 겪을 수 있다. 운동기능을 상실한 환자들이 일상 생활에서 겪는 불편함을 해결하기 위해 다양한 로봇공학 기반의 접근법이 제안되어 왔으며, 이러한 접근법은 크게 두 가지로 분류될 수 있다. 첫 번째 방법으로, 운동기능을 회복하기 위해 재활 로봇 기반의 치료를 제공할 수 있다. 재활 훈련은 물리 치료사 및 임상사의 보조로 이루어지는 것이 일반적이나, 노동력의 효율성과 반복적이고 정량적인 훈련 제공을 위하여 로봇을 이용하는 방법이 제안되고, 시도되어 왔다. 두 번째로, 운동능력의 손상 정도가 심한 경우에는 재활 훈련에 기반한 운동능력 회복에 한계가 있어, 상지의 기능을 대신할 수 있는 로봇 팔을 개발하는 것이 대안이 될 수 있다. 사람의 운동 의도가 생체신호를 통하여 분석되고, 이를 바탕으로 사용자의 의도대로 로봇 팔이 제어될 수 있다. 사람의 의도는 말단의 근육에서 전달되는 근전도 혹은 뇌에서 발생하는 뇌 신호가 활용될 수 있으며, 이러한 신호로부터 특징점을 추출하고 패턴을 인식함으로써, 의도를 분석하는 것이 일반적인 과정이다. 특히, 본 연구에서는 뇌-기계 인터페이스 기반의 제어에 초점을 맞추며, 이는 사람의 운동 신경의 신호 전달 경로를 우회할 수 있어, 적용대상이 넓은 것으로 기대된다. 특히, 팔 움직임의 상상을 통해

유도되는 비침습적 뇌 신호를 이용하여 다축 로봇 팔을 제어하는 기술은 뇌-기계 인터페이스 분야의 최종적인 목표 중 하나이다. 본 논문에서는 해당 목표에 근접하는데 기여할 수 있는 세 단계의 연구를 수행하였다.

첫 번째 단계로, 실제 팔 움직임의 손 궤적을 뇌 신호로 예측하였다. Preferred Direction 기반의 모델은 Spatial Resolution이 상대적으로 부족한 뇌전도로는 신경 단위의 신호를 측정할 수 없으므로 적용이 어렵다. 이에, 손의 속도 벡터를 추정할 수 있는 선형 모델을 활용하였다. 정상인이 손가락을 목표 물체에 도달시키고 다시 원점으로 도달하는 동작을 수행하는 동안 정상인의 뇌에서 비침습적으로 측정되는 뇌전도 혹은 뇌자도를 측정하고 이를 기반으로 같은 동작을 예측한다. 손의 궤적은 다중선형회귀 모형을 이용하여 예측되었으며, 관련 Parameter는 뇌 신호와 실제 손 궤적간의 최소자승법을 통하여 추정되었다. 실제 손의 궤적과 추정된 궤적 간의 상관계수를 계산한 결과, 뇌자도의 경우 0.705 ± 0.292 ($p < 0.001$)이며, 뇌전도의 경우 0.684 ± 0.231 ($p < 0.001$)이 도출 되었다. 로봇이 목표물체와 가장 근접한 지점에서 자동으로 Grasping 동작을 수행할 수 있도록, Preprogram되었을 때, 성공 확률은 뇌자도와 뇌전도의 경우에 각각 18.75%와 7.50%가 도출되었다. 로봇 팔의 End-Effector와 목표 물체가 접촉할 확률은 각각 52.50%와 58.75%가 도출되었다. 두 번째 단계로, 새로운 개념의 뇌-기계 인터페이스 훈련시스템을 제안하고, 개발하였다. 뇌-기계 인터페이스 훈련시스템은 사용자의 운동 상상 능력을 개선하고 Decoding Model의 Parameter를 결정하는데 활용된다. 기존의 Shared Control 기반의 훈련시스템이

우수한 훈련 효과를 보여주었지만, 위치정보가 Preprogrammed 된 물체에 한해서 적용이 되어왔다. 이에, 본 연구에서는 RGB-D Camera와 수정된 Shared Control Algorithm을 이용하여 기능을 개선하였다. 여러 개의 목표 물체를 자동으로 검출하고 그 위치를 추정할 수 있도록 하였다. 또한, Artificial Potential을 활용하여 로봇이 사용자가 의도한 물체에만 선택적으로 이끌릴 수 있도록 하였다. 이로 인해 화면에 검출된 후보물체들 중 목표물체를 사용자의 의지로 선택하고 도달할 수 있도록 개선되었다.

구현된 시스템의 목표물체 추정 오차는 $4.620 \pm 3.490\%$ 이며, 수정된 Shared Control Algorithm은 Blending Parameters $\alpha = \beta = 0.60$ 일때 사용자가 의도한 목표 물체까지의 도달오차를 51.85% 감소시킬 수 있다는 것을 Off-Line Test로 확인하였다. 마지막 단계로, 구현된 훈련시스템의 효과를 확인하기 위해 2명의 척수 손상 환자에게 적용하였다. 5 세션의 훈련을 수행한 전/후에 뇌의 기능적 자기공명영상을 촬영한 결과, 뇌의 활성화 패턴이 훈련 전과 비교하여 훈련 후에 Ipsilateral Primary Motor/Sensory Cortex, Posterior Parietal Cortex, 그리고 Contralateral Cerebellum에 집중되는 것을 확인할 수 있었다.

본 연구를 통하여 손 궤적을 예측하기 위한 선형 디코딩 모델을 검증하였으며, 영상 기반의 뇌-기계 인터페이스 훈련 시스템을 개발하였다. 또한, 개발된 훈련시스템을 척수손상환자에 적용하여 뇌의 활성화 패턴이 유의미하게 집중되는 것을 확인하였다.

핵심어: 운동 기능, 척수 손상, 뇌-기계 인터페이스, 뇌전도, 훈련 시스템, 분할 제어, 기능적 자기공명영상

학번: 2014-21552

Acknowledgement

This work was supported by the Grant (NRCTR-EX-13006, NRCTR-EX-15002, NRCTR-EX-16008) of the Translational Research Center for Rehabilitation Robots, Korea National Rehabilitation Center, Ministry of Health & Welfare, Korea, by the 2012 Seoul National University Brain Fusion Program Research Grant (800-20120444), by the BK21 PLUS Program through the National Research Foundation (NRF) funded by the Ministry of Education (22A20130011025), and by the Brain Research Program through the NRF funded by the Ministry of Science, ICT & Future Planning (2016M3C7A1904984).